



## OPEN ACCESS

## EDITED BY

Fabio Coral Fonseca,  
Instituto de Pesquisas Energéticas e  
Nucleares (IPEN), Brazil

## REVIEWED BY

Xiaohui Yan,  
Shanghai Jiao Tong University, China  
Yu-Tong Mu,  
Xi'an Jiaotong University, China

## \*CORRESPONDENCE

Pablo A. García-Salaberri,  
pagsalab@ing.uc3m.es

## SPECIALTY SECTION

This article was submitted to Fuel Cells,  
Electrolyzers and Membrane Reactors, a  
section of the journal Frontiers in Energy  
Research

RECEIVED 30 September 2022

ACCEPTED 26 October 2022

PUBLISHED 06 December 2022

## CITATION

García-Salaberri PA, Sánchez-Ramos A and  
Das PK (2022), On the optimal cathode  
catalyst layer for polymer electrolyte  
fuel cells: Bimodal pore size  
distributions with  
functionalized microstructures.  
*Front. Energy Res.* 10:1058913.  
doi: 10.3389/fenrg.2022.1058913

## COPYRIGHT

© 2022 García-Salaberri, Sánchez-Ramos  
and Das. This is an open-access article  
distributed under the terms of the [Creative  
Commons Attribution License \(CC BY\)](#). The  
use, distribution or reproduction in other  
forums is permitted, provided the original  
author(s) and the copyright owner(s) are  
credited and that the original publication in  
this journal is cited, in accordance with  
accepted academic practice. No use,  
distribution or reproduction is permitted  
which does not comply with these terms.

# On the optimal cathode catalyst layer for polymer electrolyte fuel cells: Bimodal pore size distributions with functionalized microstructures

Pablo A. García-Salaberri<sup>1\*</sup>, Arturo Sánchez-Ramos<sup>1</sup> and  
Prodip K. Das<sup>2</sup>

<sup>1</sup>Department of Thermal and Fluids Engineering, University Carlos III of Madrid, Leganés, Spain,

<sup>2</sup>School of Engineering, Newcastle University, Newcastle, United Kingdom

A high advancement has been achieved in the design of proton exchange membrane fuel cells (PEMFCs) since the development of thin-film catalyst layers (CLs). However, the progress has slowed down in the last decade due to the difficulty in reducing Pt loading, especially at the cathode side, while preserving high stack performance. This situation poses a barrier to the widespread commercialization of fuel cell vehicles, where high performance and durability are needed at a reduced cost. Exploring the technology limits is necessary to adopt successful strategies that can allow the development of improved PEMFCs for the automotive industry. In this work, a numerical model of an optimized cathode CL is presented, which combines a multiscale formulation of mass and charge transport at the nanoscale ( $\sim 10$  nm) and at the layer scale ( $\sim 1$   $\mu$ m). The effect of exterior oxygen and ohmic transport resistances are incorporated through mixed boundary conditions. The optimized CL features a vertically aligned geometry of equally spaced ionomer pillars, which are covered by a thin nanoporous electron-conductive shell. The interior surface of cylindrical nanopores is catalyzed with a Pt skin (atomic thickness), so that triple phase points are provided by liquid water. The results show the need to develop thin CLs with bimodal pore size distributions and functionalized microstructures to maximize the utilization of water-filled nanopores in which oxygen transport is facilitated compared with ionomer thin films. Proton transport across the CL must be assisted by low-tortuosity ionomer regions, which provide highways for proton transport. Large secondary pores are beneficial to facilitate oxygen distribution and water removal. Ultimate targets set by the U.S. Department of Energy and other governments can be achieved by an optimization of the CL microstructure with a high electrochemical surface area, a reduction of the oxygen transport resistance from the channel to the CL, and an increase of the catalyst activity (or maintaining a similar activity with

Pt alloys). Carbon-free supports (e.g., polymer or metal) are preferred to avoid corrosion and enlarge durability.

#### KEYWORDS

catalyst layer, Pt loading, transport, optimization, performance, durability, proton exchange membrane fuel cell, fuel cell vehicle

## 1 Introduction

The development of thin-film catalyst layers (CLs) at Los Alamos National Laboratory (LANL) at the beginning of the 90s (thickness,  $\delta_{cl} \approx 50\text{--}100\ \mu\text{m}$ ) was a breakthrough in proton exchange membrane fuel cells (PEMFCs). The replacement of microstructures that worked with liquid electrolytes based on Pt black catalyst and polytetrafluoroethylene (PTFE) binder by microstructures based on Pt/C catalyst and ionomer (Nafion) dramatically increased catalyst utilization, decreasing Pt loading from  $L_{Pt} = 4\ \text{mg}_{Pt}\ \text{cm}^{-2}$  to  $L_{Pt} = 0.4\ \text{mg}_{Pt}\ \text{cm}^{-2}$  (Wilson and Gottesfeld, 1992). However, Pt loadings around  $L_{Pt} = 0.4\ \text{mg}_{Pt}\ \text{cm}^{-2}$  are still the commercial standard, since a further reduction of the Pt loading has been difficult since then due to performance and durability issues (Kongkanand and Mathias, 2016; Nguyen et al., 2021; Tellez-Cruz et al., 2021). Losses are more important at the cathode due to the sluggish kinetics of the oxygen reduction reaction (ORR) and lower diffusivity of oxygen compared with the fast kinetics of the hydrogen oxidation reaction (HOR) and high diffusivity of hydrogen (García-Salaberrí, 2022). Concern about this situation has increased in the last decade as PEMFCs are reaching their commercialization stage, especially in the automotive sector, where they compete with other technologies (internal combustion engine and Li-ion battery) (Atanassov et al., 2021). Recent targets set by the U.S. Department of Energy (DOE) for fuel cell vehicles to make PEFC technology competitive have been hardly met (Wang et al., 2020a). The Toyota Mirai presented in 2018 showed limited durability of 3,000 h in a real-world driving test and failed largely in a DOE accelerated stress test (AST) protocol. The performance decreased significantly after 5,000 cycles with a cathode CL thickness reduction from approximately  $10\ \mu\text{m}$ – $3\ \mu\text{m}$  (Borup et al., 2018). Recently, an assessment performed by a team of experts concluded that the median 2017 automotive cost of a PEMFC system is around  $75\ \$\ \text{kW}^{-1}$  with a stack durability and power density of 4,000 h and  $2.5\ \text{kW L}^{-1}$ , whilst the DOE ultimate targets are  $30\ \$\ \text{kW}^{-1}$ , 8,000 h and  $3\ \text{kW L}^{-1}$ , respectively. The ultimate performance target is expected to be met by 2035 and the ultimate cost and durability targets by 2050 (Whiston et al., 2019). Despite the ongoing progress, other numbers are also still away of targets established for 2025 by the U.S. and other regions, such as the European Union (Yunzhe et al., 2020) (the status reported during 2015–2020 is indicated in brackets (DOE, 2015;

Wang et al., 2020a)): 1) total Pt group metal (PGM) content lower than  $0.1\ \text{g}\ \text{kW}^{-1}$  ( $0.16\ \text{g}\ \text{kW}^{-1}$ ); 2) rated power density of  $1\ \text{W}\ \text{cm}^{-2}$  ( $0.81\ \text{W}\ \text{cm}^{-2}$ ); 3) minimum electrical resistance of  $1000\ \Omega\ \text{cm}^2$  ( $1635\ \Omega\ \text{cm}^2$ ).

A key issue for decreasing Pt loading (mainly at the cathode) is caused by local mass transport resistance introduced by thin ionomer films surrounding Pt nanoparticles (Weber and Kusoglu, 2014; Sánchez-Ramos et al., 2021, 2022). The local oxygen transport resistance (per unit of geometric area) is inversely proportional to the roughness factor, the ratio between the electrochemically active surface area and the cell geometric area,  $r_f = A_{Pt} A_{geo}^{-1}$ . The detrimental effect of reducing  $r_f$  is a limitation of heterogeneous reactive systems, since the average oxygen flux at the surface of Pt nanoparticles,  $N_{O_2}^{Pt}$ , increases by a factor  $r_f^{-1}$  with respect to the oxygen flux per unit of geometric area,  $N_{O_2}^{geo}$ . In other words,  $N_{O_2}^{Pt} = r_f^{-1} N_{O_2}^{geo}$  according to the species mass conservation equation (Greszler et al., 2012). For a vanishing Pt loading ( $L_{Pt} \rightarrow 0$ ), the oxygen flux at a lonely catalytic site would become infinitely high,  $N_{O_2}^{Pt} \rightarrow \infty$ , thereby leading to strong mass transport losses to maintain a prescribed current density ( $I^{avg} > 0$ ). Consequently, the cell performance will inevitably drop to the stable point provided by a null current density ( $I^{avg} \rightarrow 0$  when  $r_f \rightarrow 0$ ) regardless of the feed flow rate and the catalyst activity. A similar barrier would arise for other transported species, protons and electrons, even though the performance limitation is less severe than in the case of oxygen because charge transport resistances are lower, especially in the case of electrons. The performance loss at small  $r_f$  can be mitigated in three ways: 1) increasing the electrochemically active surface area per unit catalyst mass, ECSA, to increase  $A_{Pt}$  at a given Pt loading,  $L_{Pt}$ , 2) reducing any mass transport resistance in the path of oxygen from the channel (say, stack inlet) toward each catalyst site, and 3) increasing the catalyst mass activity, so that each Pt nanoparticle can potentially generate a higher current at a given overpotential (provided that other losses do not limit performance). If the design is not restricted to Pt, the fourth 4) available option is to use Pt alloys or PGM-free catalysts with an activity comparable to that of Pt (Sánchez-Ramos et al., 2022; Liu et al., 2019b,a).

A large effort has been devoted to improving performance at low Pt loading, including the increase of the ECSA, the development of more active catalysts with reduced Pt content, and the decrease of mass transport resistances in the membrane electrode assembly (MEA), flow field and

stack (Goshtasbi et al., 2019; Park et al., 2019; Chen et al., 2020; Cochet et al., 2020). Here, we shall focus mainly on the latter approach, since the other options can be incorporated into a previously optimized design in terms of mass transport. Reducing the oxygen transport resistance in a PEMFC can be addressed by: 1) a reduction of the internal mass transport resistance of the CL microstructure, 2) a reduction of the mass transport resistance of the backing layer (gas diffusion layer, GDL, and microporous layer, MPL) and at the GDL/channel/rib interface, 3) a decrease of the along-the channel and stack flow distributor resistance caused by difficulties in liquid water removal (especially at high current densities above 2–3 A cm<sup>-2</sup>), or a combination thereof (see, e.g. (Yi et al., 2012; Choi et al., 2014; García-Salaberri P. et al., 2017; Azarafza et al., 2019; Deng et al., 2021; Zhang et al., 2021; Zapardiel and García-Salaberri, 2022), among others). The ohmic loss in the proton exchange membrane (PEM) and CLs is less relevant at low Pt loading in state-of-the-art designs. **Figure 1A** shows the peak power density per unit mass of Pt achieved with some CL designs presented in the last years. To facilitate the presentation, two groups are distinguished: 1) conventional CLs (CONV and C-ENG in **Figure 1**) based on the original thin-film CL design without and with engineered or modified nanoporous supports (pore radius,  $R_p \leq 10$  nm), and 2) innovative CLs (VA, NSTFC and I-ENG in **Figure 1**), which includes alternative CL designs aimed at reducing mass and ohmic transport losses across the CL thickness, at local Pt sites, or at both locations. Advances achieved in both groups are discussed below.

In terms of conventional CLs, two main approaches have been used to enhance performance at low Pt loading: 1) reduction of bulk transport losses considering alternative production techniques (e.g., catalyst deposition by electrospraying or freeze drying (Folgado et al., 2018; Talukdar et al., 2019)), and 2) the modification of nanoporous supports to optimize triple phase points at catalyst sites (CONV-ENG) (Yarlagadda et al., 2018; Ramaswamy et al., 2020; Kobayashi et al., 2021). The second strategy is more fundamental. Provided that a continuous electron pathway exists across a CL, there are two options to form triple phase points (allowing a simultaneous access of oxygen, protons and electrons): 1) active catalyst in contact with liquid water, and 2) active catalyst in contact with hydrated ionomer. Compared with transport in an ionomer film, oxygen diffusion in liquid water is easier while proton conduction in liquid water is more difficult (Zenyuk and Litster, 2014; Muzaffar et al., 2018). Since oxygen transport is typically the limiting process at low Pt loading, transport in liquid water at triple phase points is preferred (Yarlagadda et al., 2018). In addition, catalyst sites in contact with liquid water do not suffer from a reduction of the electrochemical activity due to adsorption of sulfonate groups at hydrophilic Pt surfaces (Takeshita et al., 2020). The General

Motors Company exploited this approach by engineering accessible nanopores already present in high surface area carbon (HSAC) supports, such as Ketjenblack, in contrast to low surface area carbon (LSCA) supports (e.g., Vulcan) (Yarlagadda et al., 2018). Van der Waals adsorption, capillary condensation and water generation ensured the presence of liquid water in nanopores. As a result, efficient oxygen and proton transport around catalyst sites was possible, while providing good proton transport at the layer scale through ionomer films (Zenyuk and Litster, 2014). The achieved Pt mass-specific performance was remarkably high (the largest reported so far to the authors' knowledge),  $P_{Pt} \approx 20$  W mg<sub>Pt</sub><sup>-1</sup> ( $I^{avg} = 2$  A cm<sup>-2</sup> at  $V_{cell} \approx 0.65$  V and  $L_{Pt} = 0.06$  mg<sub>Pt</sub> cm<sup>-2</sup>), similar to that reached in the Toyota Mirai with  $L_{Pt} = 0.3$  mg<sub>Pt</sub> cm<sup>-2</sup> (five times higher). Generally speaking, for a given nanoporous support and CL preparation route, a fraction of Pt nanoparticles is deposited inside nanopores, while the remaining stays on the outer surface covered by ionomer. Consequently, there is an optimum ionomer-to-carbon ratio,  $I/C^{opt}$ , which maximizes the peak power density due to a proper balance between mass transport and ohmic losses. When most of the catalyst is inside nanopores, a higher I/C is desirable to facilitate proton transport along the outer surface if ionomer does not block the access to the interior of nanopores (Kobayashi et al., 2021).

In terms of innovative CLs, Toyota Motor Corporation developed vertically aligned (VA) microstructures based on the idealized design proposed by Middelmann (Middelmann, 2002; Murata et al., 2014). This idealized microstructure is composed of a structured array of electron-conductive pillars catalyzed with Pt and covered with a co-axial ionomer film for proton transport. This design provides the best theoretical solution to minimize bulk transport losses provided that water flooding is not an issue and the ionomer film is able to conduct protons efficiently with a negligible local mass transport resistance. However, this is not usually the case in practice, where the ionomer mass transport resistance significantly reduces the performance at low Pt loading, leading to a non-optimal ECSA utilization (Spingler et al., 2017; Schuler et al., 2019). Two worth noting designs have been proposed to overcome this issue: 1) ionomer-free nanostructured thin film catalyst (NSTFC) developed by The 3M Company (Debe et al., 2006; Debe, 2011; Debe et al., 2011; Debe, 2012; Ostroverkh et al., 2019), and 2) designs based on a combination of ionomer nanofibers (proton transport highways) and a conventional microstructure with reduced ionomer content (ION-ENG) examined by U.S. National Laboratories and Toyota Motor Corporation (Zhang and Pintauro, 2011; Borup and Weber, 2019; Sun et al., 2019; Yoshino et al., 2020). Ultra-thin NSTFC electrodes ( $\delta_{cl} < 1$  μm) are solely composed of polymer whiskers catalyzed by a Pt monolayer, so that the Pt skin is used to conduct electrons and (generated) liquid water to conduct protons. Despite its simplicity, the main drawback of this design is caused by flooding of the cathode

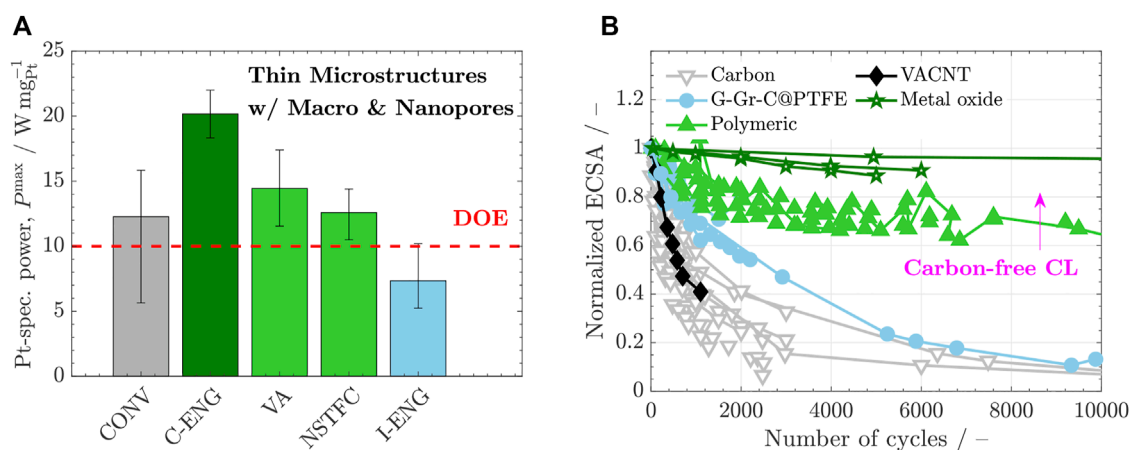


**FIGURE 1**

(A) Peak power per Pt milligram,  $P_{\max}$ , achieved with different cathode CL designs: CONV, conventional CLs with solid (Vulcan) and nanoporous (e.g., KetjenBlack) carbon supports prepared by different techniques (e.g., airbrush or electrospaying) (Orfanidi et al., 2017; Garsany et al., 2018; Conde et al., 2019; Talukdar et al., 2019; Cui et al., 2021); CONV-ENG, conventional CLs with engineered or modified nanoporous supports (Yarlagadda et al., 2018; Ramaswamy et al., 2020); VA, CLs with vertically aligned supports covered by ionomer (i.e., based on Middelmann's ideal microstructure) (Murata et al., 2014; Xia et al., 2015; Meng et al., 2022); NSTFC, ionomer-free nanostructured thin film catalysts (Debe (2012); Debe et al. (2011); Debe (2011); Debe et al. (2006); Ostroverkh et al. (2019)); ION-ENG, CLs with engineered or modified ionomer distributions (e.g., a combination of ionomer nanofibers and conventional microstructures with reduced ionomer content) (Zhang and Pintauro, 2011; Borup and Weber, 2019; Sun et al., 2019; Yoshino et al., 2020). The 2020 DOE target,  $P \approx 10 \text{ W mg}_{\text{Pt}}^{-1}$ , is indicated by a red dashed line. Baseline operating conditions: air/ $\text{H}_2$ , temperature,  $T = 70 - 80^\circ\text{C}$ , relative humidity,  $RH = 1$ , cathode back pressure,  $p_c = 150 \text{ kPa( abs)}$ . (B) Normalized ECSA with respect to BOL as a function of the number of cycles in ASTs for different catalyst supports: Carbon, CLs supported on conventional carbon nanoparticles ((Babu et al., 2021) and other references included herein); G-Gr-C@PTFE, CLs supported on either graphitized carbon, graphene or PTFE-doped carbon nanoparticles (Wang et al., 2019; Babu et al., 2021; Pushkareva et al., 2021); VACNT, CLs based on vertically aligned carbon nanotubes covered by ionomer (Murata et al., 2014; Meng et al., 2022); Polymer, CLs based on polymer whiskers without (e.g., NSTFC (Debe et al., 2006; Debe, 2011; Debe et al., 2011; Debe, 2012; Ostroverkh et al., 2019)) and with (Xia et al., 2015) ionomer films; Metal oxide, conventional CLs supported on metal oxide nanoparticles (e.g., titanium dioxide ( $\text{TiO}_2$ ) powder) (Esfahani et al., 2018; Esfahani and Easton, 2020; Chen et al., 2021).

CL at low operating temperature, which can be ascribed to the hydrophilicity of the Pt skin and CL thinness (Debe, 2012; Zenyuk et al., 2016a). Moreover, oxygen diffusion and proton conduction across hundreds of nanometers of liquid water in NSTFC electrodes is a sub-optimal solution to increase the peak power density compared with the lower lengths that can be achieved in CON-ENG designs. ION-ENG electrodes are an interesting option toward the development of bi-functionalized microstructures that can combine facilitated domains for oxygen and proton transport. Currently, the main practical difficulty lies in producing composite microstructures with a good transition between ionomer nanofibers and ionomer thin films. The performance achieved with this variant is still below the 2020 DOE target, even though it has been shown to be a viable route to increase performance at reduced RH due to enhanced water uptake (Yoshino et al., 2020).

The ECSA reduction normalized with respect to the value at the beginning of life (BOL) achieved in ASTs with different catalyst supports is shown in Figure 1B. Although the high activity of Pt/C catalysts is desirable, carbon supports can suffer from limited durability mainly due to: 1) agglomeration of Pt nanoparticles ( $R_{\text{Pt}} \sim 2 \text{ nm}$ ) caused by electrochemical

Ostwald ripening and/or migration-coalescence, and 2) an overlap between the operating voltage and the carbon corrosion potential, especially at cell voltages above  $V_{\text{cell}} \approx 1 \text{ V}$  (Babu et al., 2021; Zhao et al., 2021). Catalyst agglomeration leads to a direct reduction of the ECSA, since larger Pt nanoparticles feature a lower specific surface area,  $\text{ECSA} \propto R_{\text{Pt}}^{-1}$ . An effective strategy to mitigate catalyst agglomeration is the use of stable catalyst skins, which behave as one being rather than as multiple independent entities (Debe et al., 2006; Mardle and Du, 2022). Carbon corrosion leads to a loss of support material due to carbon oxidation, which causes electrode thinning, porosity reduction, pore size increase (reduction of nanopore volume fraction) and ECSA reduction (Borup et al., 2020). The combined effect of material loss and nanopore clogging can be particularly problematic for HSAC supports that store a large part of their ECSA inside nanopores. Recent work has shown that the durability of carbon-based supports can be somewhat extended using graphitized carbon or graphene, as well as carbon supports doped with tailored amounts of PTFE, because of their higher oxidation resistance (Wang et al., 2019; Babu et al., 2021; Pushkareva et al., 2021). Vertically aligned carbon nanotubes (VACNTs) also seem

## Bi – functionalized Bimodal Microstructure

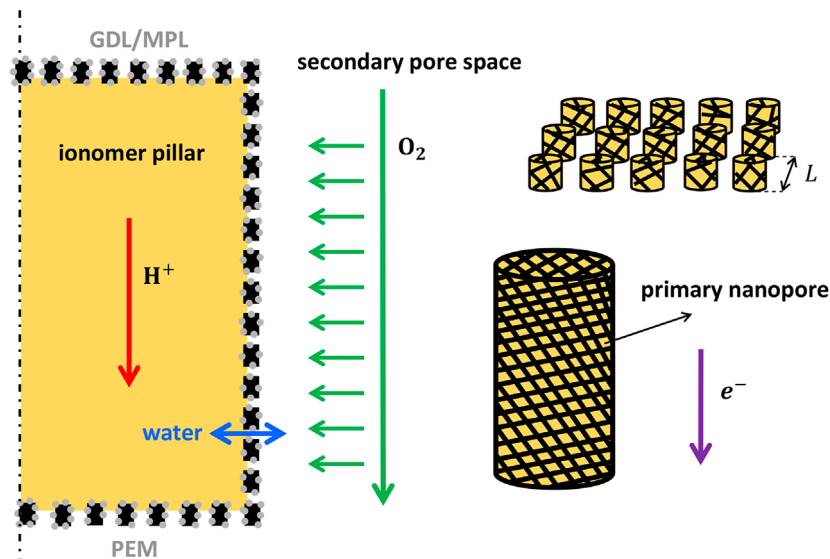


FIGURE 2

Schematic of a bi-functionalized bimodal cathode CL microstructure with targeted domains for proton and gas species transport, and a primary ( $R \leq 10$  nm)/secondary ( $R \geq 10$  nm) pore size distribution. ORR and electron transport take place in a nanoporous shell covering ionomer pillars, which is made of a highly electron-conductive material catalyzed with Pt. Liquid water can be transported both through ionomer pillars and released to secondary pores. The characteristic spacing between pillars is  $L$ .

to be an insufficient solution to solve the problem of carbon corrosion (Murata et al., 2014; Meng et al., 2022), even though improvement has been achieved with double-walled (DWCNTs) and multi-walled (MWCNTs) carbon nanotubes (Chen et al., 2007; MoghadamEsfahani et al., 2020). Carbon-free electrodes have shown significantly longer durability than carbon-based supports due to oxidation suppression (Antolini and Gonzalez, 2009; Lv and Mu, 2014). Among carbon-free supports, metal oxide supports are a robust option because of their high electrical conductivity and corrosion resistance. In particular, titanium dioxide ( $\text{TiO}_2$ ) supports are very active with Pt and have provided an extraordinarily high corrosion resistance above DOE targets (Esfahani et al., 2018; Esfahani and Easton, 2020; Chen et al., 2021). Nevertheless, the widespread adoption of supports based on Ti requires an economic analysis. Polymeric and ceramic supports can be a cost-effective alternative but in general suffer from the problem of low electrical conductivity, being necessary a modification of the raw material (Xia et al., 2015). The issue of low electrical conductivity can be avoided if the support is not used for electron conduction, as in the case of NSTFC electrodes (Debe, 2012).

In this work, as shown in Figure 2, the performance of an idealized cathode CL which features a VA geometry with a bimodal pore size distribution is examined. The microstructure is fully bi-functionalized, so there is no interaction between the ionomer space devoted to proton transport and the secondary

space devoted to oxygen transport. The ORR takes place in water-filled primary nanopores grooved in an electron-conductive shell in contact with both domains, and catalyzed with an atomic Pt skin to maximize the ECSA. This microstructure provides an idealized version of the situation found in engineered HSAC supports (CONV-ENG) in which the solid volume fraction has been minimized with the aim of providing a continuous path for electron transport without a significant electrical loss (Wilson and Gottesfeld (1992)). The design further considers that all nanopores (i.e., Pt sites) are accessible and removes entirely any ionomer transport resistance at the entrance of nanopores. The proposed microstructure is to be optimized geometrically. The organization of the paper is as follows. In Section 2, the assumptions and the multiscale approach considered to model the idealized cathode CL and exterior mass and ohmic transport resistances are presented. A special focus is devoted in Subsection 2.1 to the assumptions made on water management, which has not been explicitly modeled here. The formulations of the macroscopic model at the layer scale and the microscopic model at the nanopore scale are presented in Sections 3 and 4, respectively. The case studies are described in Section 5, which considers an analysis of the optimized geometry of the idealized cathode CL, the effect of exterior transport resistances, and the effect of catalyst activity. The results are discussed in Section 6, where technological frontiers are analyzed. Finally, the conclusions are presented in Section 7.



## 2 Numerical model

### 2.1 Assumptions

The main simplifying assumptions adopted in the model formulation are as follows:

- 1) Steady state operation, isothermal conditions and ideal gases.
- 2) Full gas humidification ( $RH_a^{in} = RH_c^{in} = 1$ ) and temperature operation at  $T \approx 80^\circ\text{C}$ .
- 3) The PEM is perfectly impermeable to gas species and convection is negligible in the CL.
- 4) Adsorption kinetics at catalyst sites for the examined voltage close to peak power density ( $V_{\text{cell}} = 0.5\text{ V}$ ) is infinitely fast (Sánchez-Ramos et al., 2021).
- 5) The oxygen concentration drop from the channel to the CL/MPL interface and the voltage drop in other components different from the cathode CL are quantified by an overall mass transport resistance,  $R_{\text{O}_2}^{\text{chcl}}$ , and an overall area-specific ohmic resistance,  $\text{ASR}_{\text{pem}}$ , respectively. Both resistances do not vary with current density.
- 6) Ohmic and thermal contact resistances are negligible.
- 7) The CL microstructure is macroscopically homogeneous, being composed of evenly spaced ionomer pillars covered by a nanoporous electron-conductive shell. The interior surface of nanopores is catalyzed with an atomic Pt skin, and the solid fraction of the shell is composed of a highly conductive material, such as graphite ( $\sigma_e \sim 10^4\text{ S cm}^{-1}$ ), graphene ( $\sigma_e \sim 10^5\text{ S cm}^{-1}$ ) or a metal (e.g., Ti,  $\sigma_e \sim 10^4\text{ S cm}^{-1}$ ). The secondary pore space between ionomer pillars shows a uniform pore size distribution (rather than a heterogeneous pore size distribution as in conventional CLs (Sakai et al., 2009)).
- 8) Degradation is negligible and the stiffness of the CL is infinitely high (Jomori et al., 2012).
- 9) The CL temperature is high enough to avoid flooding due to electrochemical generation and net water transport from anode to cathode. The secondary pore space is partially saturated with a prescribed average saturation  $s_{\text{avg}}$ , which is used to correct the bulk effective diffusivity. Two-phase flow of water saturation and water vapor is not modeled (see below).
- 10) Primary nanopores grooved in the electron-conductive shell are filled with liquid water from the ORR due to Van der Waals adsorption, capillary condensation and Knudsen effect.

The last two assumptions deserve further attention. Unlike porous media with pore sizes larger than  $1\text{ }\mu\text{m}$ , two-phase transport in a CL is affected by two nanoscale aspects: 1) reduction of the vapor pressure of water by Van der Waals adsorption and Kelvin effect, and 2) reduction of the diffusivity coefficient of gas species by Knudsen effect.

According to the Kelvin equation, the actual saturation pressure of water in a nanometric concave meniscus,  $p_{\text{H}_2\text{O}}^{\text{sat}}$ , is reduced exponentially compared with the value of a flat interface,  $p_{\text{H}_2\text{O}}^{\text{sat,flat}}$ , according to

$$\ln\left(\frac{p_{\text{H}_2\text{O}}^{\text{sat}}}{p_{\text{H}_2\text{O}}^{\text{sat,flat}}}\right) = -\frac{2\sigma V_{m,\text{H}_2\text{O}}}{R^{\text{eff}}R^o T} \quad (1)$$

where  $R^o$  is the universal gas constant,  $\sigma \approx 0.072\text{ Nm}^{-1}$  is the surface tension of the water-air fluid pair,  $V_{m,\text{H}_2\text{O}} = M_{\text{H}_2\text{O}}/\rho_{\text{H}_2\text{O}}$  is the molar volume of water,  $R^{\text{eff}} = R/\cos\theta$  is the (effective) meniscus radius, and  $\theta$  is the contact angle. Water shows a hydrophilic or mixed-wettability character with conventional materials employed in CLs ( $\theta \leq 90^\circ$ ). The contact angle is lower for metals, such as Pt, stainless steel and  $\text{TiO}_2$  ( $\theta_{\text{Pt}} \approx 40^\circ$ ,  $\theta_{\text{ss}} \approx 65^\circ$ ,  $\theta_{\text{TiO}_2} \approx 72^\circ$ ), and higher for carbon ( $\theta_c \approx 80^\circ$ ) (Park and Aluru, 2009; Martinez-Urrutia et al., 2018; Liu et al., 2021). Hydrophobic contact angles can be achieved with graphene ( $\theta_{\text{gr}} \approx 95^\circ - 100^\circ$ ) (Taherian et al., 2013).

The reduction of the diffusivity coefficient of species  $i$  due to Knudsen effect (i.e., the frequent collision of gas molecules with pore walls) depends on the pore radius,  $R$ , according to the expression

$$f^{\text{knud}} = \frac{D_i}{D_i^{\text{mol}}} = \left(1 + \frac{D_i^{\text{mol}}}{D_i^{\text{knud}}}\right)^{-1} \quad (2)$$

where  $D_i^{\text{mol}}$  is the molecular diffusivity coefficient,  $D_i$  is the apparent diffusivity coefficient, which can be approximated by the Bosanquet formula, and  $D_i^{\text{knud}}$  is the Knudsen diffusivity, given by the kinetic theory of gases

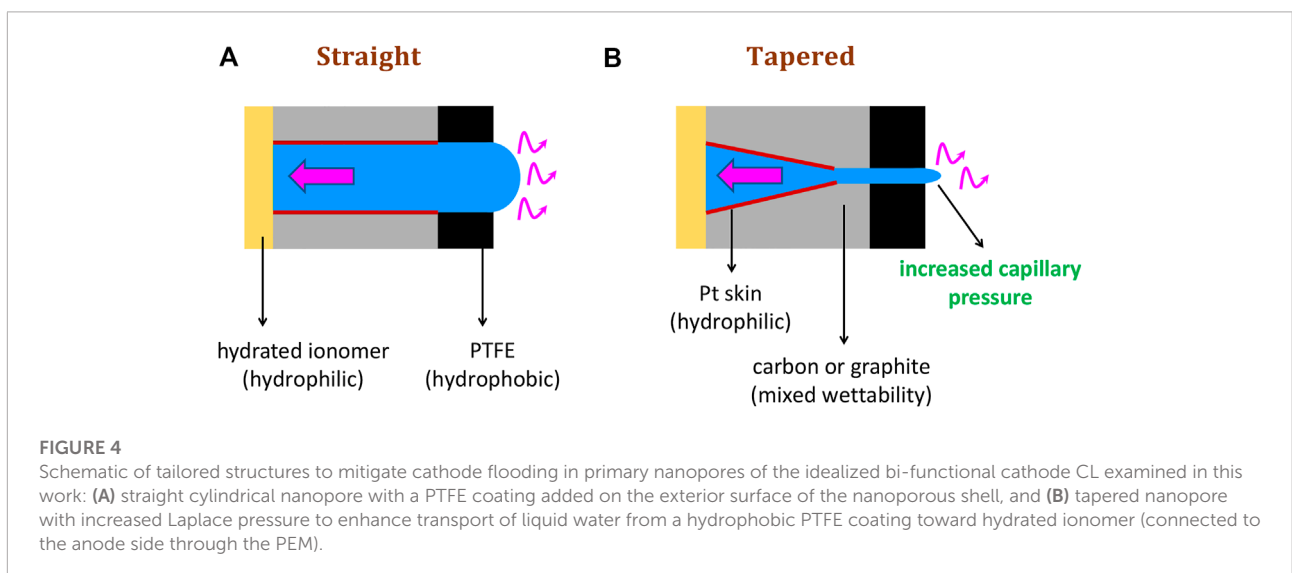
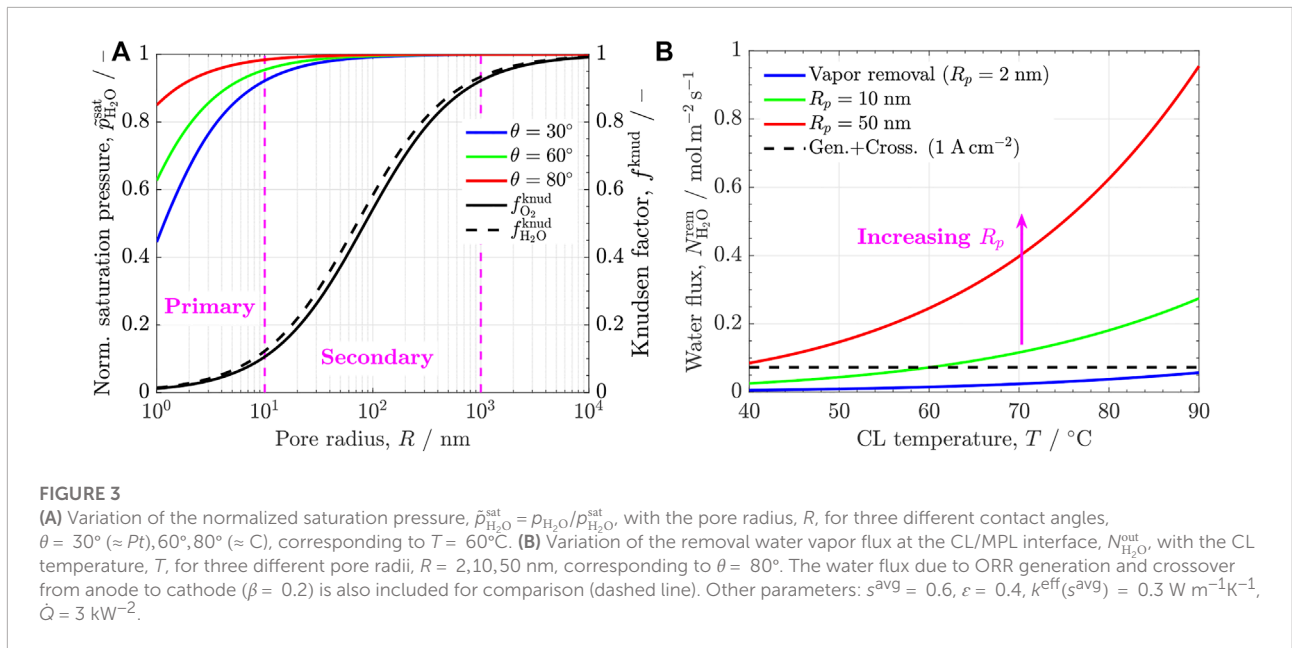
$$\frac{1}{D_i} = \frac{1}{D_i^{\text{mol}}} + \frac{1}{D_i^{\text{knud}}}; \quad D_i^{\text{knud}} = \frac{R}{3} \sqrt{\frac{8R^o T}{\pi M_i}} \quad (3)$$

with  $M_i$  the molecular mass of species  $i$ .

Four key characteristic times can be distinguished related with two-phase transport in the pore space of a CL: 1) capillary action estimated according to the Young-Laplace equation,  $t_c$ , 2) phase change of water from the Hertz-Knudsen equation (Jiao and Li, 2011; Attari Moghaddam et al., 2017),  $t_{pc}$ , 3) viscous transport of liquid water from the Navier-Stokes equations,  $t_v$ , and 4) diffusion of water vapor from Fick's law,  $t_{\text{H}_2\text{O},d}$ . For a pore radius  $R \sim 50\text{ nm}$  and a characteristic velocity  $v_c \sim (I^{\text{avg}}/2F)(M_{\text{H}_2\text{O}}/\rho_{\text{H}_2\text{O}}) \sim 10^{-6}\text{ s}$  at  $I^{\text{avg}} \approx 1\text{ A cm}^{-2}$ , the estimated times in increasing order are.

$$t_c = \frac{\rho v_c R^2}{\sigma} \sim 10^{-17}\text{ s} \quad (4a)$$

$$t_{pc} = \frac{1}{a_{lv} \sqrt{\frac{R^o T}{2\pi M_{\text{H}_2\text{O}}}}} \sim 10^{-12}\text{ s} \quad (4b)$$



$$t_v = \frac{R^2}{\nu} \sim 10^{-9} \text{ s} \quad (4c)$$

$$t_{\text{H}_2\text{O},d} = \frac{R^2}{D_{\text{H}_2\text{O}}^{\text{eff}}} \sim 10^{-10} \text{ s} \quad (4d)$$

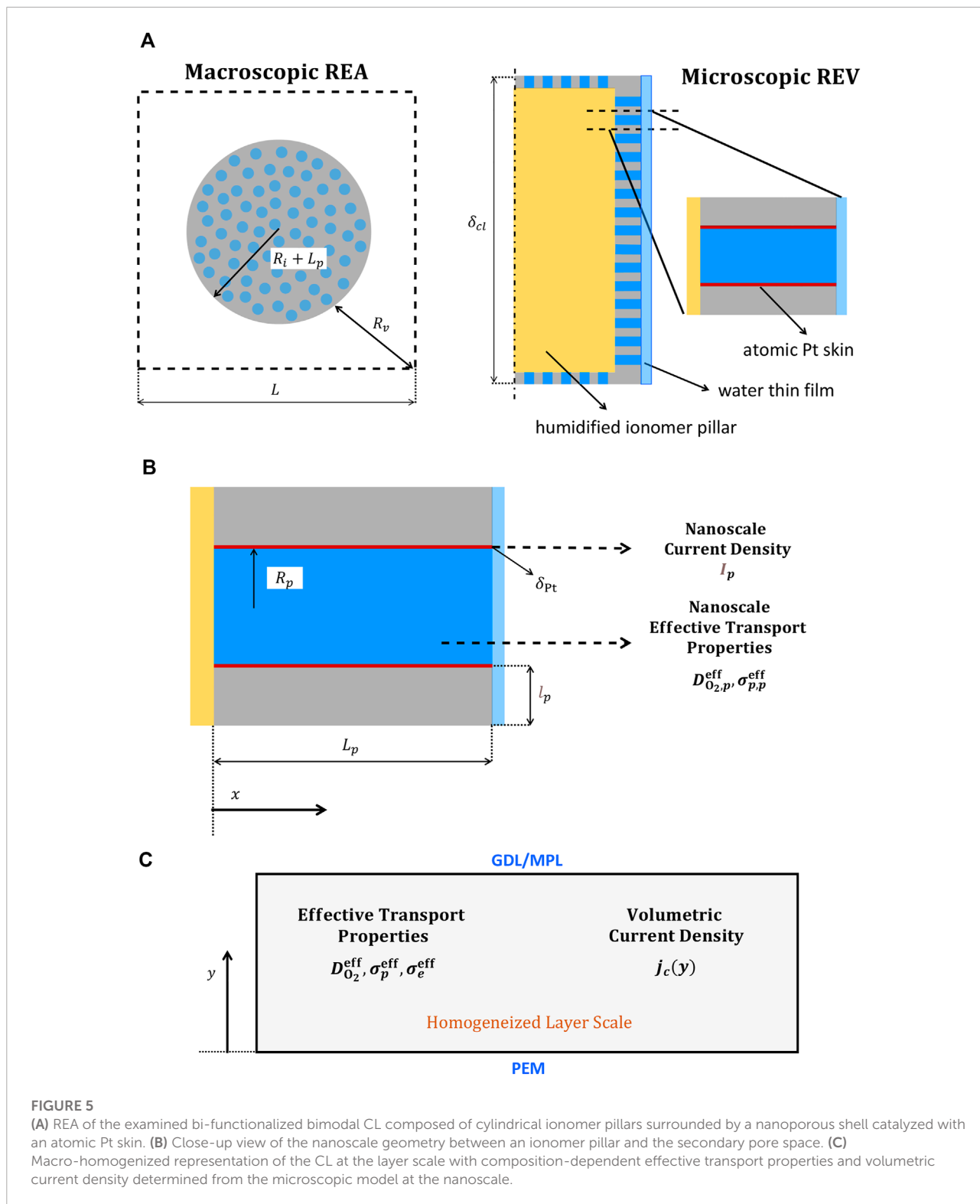
where  $a_{lv}$  is the liquid-water specific surface area, which is in the order of  $a_{lv} \sim R^{-1} \sim 2 \times 10^7 \text{ m}^{-1}$  for  $R = 50$  nm, and  $\rho \approx 10^3 \text{ kg m}^{-3}$  and  $\nu \approx 10^{-6} \text{ m}^2\text{s}^{-1}$  are the density and the kinematic viscosity of liquid water, respectively. The effective diffusivity of water vapor,  $D_{\text{H}_2\text{O}}^{\text{eff}}$ , for a conventional CL can be approximated as,  $D_{\text{H}_2\text{O}}^{\text{eff}} = D_{\text{H}_2\text{O}}^{\text{mol}} f^{\text{knud}} f^{\text{obs}}$ , with  $f^{\text{obs}} = \varepsilon^2 (1 - s^{\text{avg}})^{2.5}$  ( $\varepsilon \approx 0.4$ ,  $s^{\text{avg}} \approx 0.4$ ) and  $D_{\text{H}_2\text{O}}^{\text{mol}}(T) = 2.98 \times$

$10^{-5}(T/333)^{1.5}$  ( $T = 80^\circ\text{C}$ ) (Sánchez-Ramos et al., 2021; García-Salaberri, 2022).

The liquid-phase pressure drop needed to drive the flow of liquid water across a CL can be estimated from Darcy's law. Considering a CL permeability,  $K \sim 10^{-15} - 10^{-16} \text{ m}^2$ , and a thickness,  $\delta_{cl} \sim 5 \mu\text{m}$  (Zhao et al., 2018), we yield

$$\Delta p_l \sim \frac{\mu \nu_c \delta_{cl}}{K} \sim 1 - 10 \text{ Pa} \ll p_c \sim \frac{\sigma}{R^{\text{eff}}} \sim 10^4 \text{ Pa} \quad (5)$$

According to this result, the effect of the liquid water flow on the liquid pressure distribution established by capillarity is virtually negligible, which agrees with the numerical results of Liu et al. (2013) and previous experimental  $p_c$ - $s$  curves reported for CLs without and with cracks Kusoglu et al. (2012).





Putting all together, the above estimations suggest that water transport in vapor and liquid forms take place on a time scale significantly slower than phase change phenomena and (virtually instantaneous) capillary action (i.e.,  $t_v, t_{H_2O,d} \gg t_{pc} \gg t_c$ ). Water transport is also expected to be slower compared with water desorption/sorption from/to ionomer, since ionomer and liquid-water specific surface areas are of a similar order of magnitude in conventional CLs ( $a_{lv} \sim a_i \sim R^{-1}$ ). This scenario is comparable to that reported for GDLs, where evaporation/condensation of water is controlled by transport rather than interfacial kinetics (Gebel et al., 2011; Fumagalli et al., 2015; Zenyuk et al., 2016b). As shown in **Figure 3A**, the bimodal pore size distribution of CLs offers a good balance to simultaneously provide a high liquid-gas interfacial area in water-filled primary pores due to Van der Waals adsorption and capillary condensation ( $R \sim 2\text{--}10\text{ nm}$ ), and an enhanced water vapor removal rate through secondary pores due to reduced Knudsen effect ( $R \geq 50\text{ nm}$ ) (Zientara et al., 2013; Li et al., 2019; Huang et al., 2021). Neglecting phase-change resistances, the water vapor removal rate under partially-saturated conditions driven by a temperature gradient across a CL is given by (Kim and Mench, 2009)

$$N_{H_2O}^{out} = \frac{1}{R^o} \frac{d(D_{H_2O}^{eff} P_{H_2O}^{sat}/T)}{dT} \frac{dT}{dz} \quad (6)$$

where  $P_{H_2O}^{sat}(T)$  is the saturation pressure of water (Sánchez-Ramos et al., 2021). This expression shows that although CLs are almost isotherms (temperature variation,  $\Delta T \lesssim 10^{-3} - 10^{-2}\text{ K}$ ), the temperature gradient created by generated heat is similar to that found in GDLs and cannot be neglected. In a first approximation, neglecting the water vapor flux across the PEM, the temperature gradient at the CL/MPL interface increases with current density

$$\frac{dT}{dz} \sim \frac{\Delta T_{cl}}{\delta_{cl}} \sim \frac{\dot{Q}}{k^{eff}(s^{avg})}; \quad \dot{Q} \sim \frac{1}{2} \left( \frac{h_{lv}}{2F} - V_{cell} \right) I^{avg} \quad (7)$$

where  $\dot{Q}$  is the heat flux removed through the cathode compartment due to electrochemical reaction at a current density  $I^{avg}$ , which can be reasonably assumed to be half of the total generated heat flux,  $h_{lv} \approx 242\text{ kJ mol}^{-1}$  is the latent heat of vaporization/condensation of water,  $V_{cell}$  is the operating cell voltage and  $F$  is Faraday's constant (Thomas et al., 2014; Straubhaar et al., 2015).

**Figure 3B** shows the water vapor removal rate as a function of CL temperature for various pore radii, corresponding to an output current density  $I^{avg} \approx 1\text{ A cm}^{-2}$  and a net water transport coefficient across the PEM from anode to cathode,  $\beta = 0.2$  ( $s^{avg} \approx 0.6$ ). For a small pore radius,  $R \approx 2\text{ nm}$ , the water removal flux in vapor form is not sufficient to transport the generation + crossover water flux in the temperature range  $T = 40\text{--}90^\circ\text{C}$ . The same situation is found at temperatures below  $T \leq 60^\circ\text{C}$  for  $R \approx 10\text{ nm}$ . Consequently, excess water is

removed to the cathode MPL in liquid phase, condensed in the pore space, sorbed into the ionomer and/or pushed to the anode by a pressure difference (if a pressure difference between compartments exists). In contrast, when the pore radius is increased to tens of nanometers,  $R \geq 50\text{ nm}$ , removal in vapor form is possible in the full temperature range. As a result, liquid water is desorbed from the ionomer to the pore space, liquid water is evaporated and/or liquid water enters the cathode CL by a pressure difference. This result highlights the importance of maintaining the CL at as high a temperature as possible within operational constraints. For a given current density (i.e., heat flux,  $\dot{Q}$ ), liquid water saturation in the cathode CL can be decreased in three (main) ways: 1) reducing the water crossover flux from anode to cathode (e.g., using a hydrophobic cathode CL and/or a thin PEM), 2) enhancing water removal in vapor form with a lower effective thermal conductivity under partially saturated conditions and/or increasing the CL temperature (regardless of the cell temperature), and 3) facilitating water removal in liquid form, so that water that cannot be vaporized or sorbed to the ionomer can be easily evacuated in liquid form (Avcioglu et al., 2016; Chi et al., 2018; Folgado et al., 2018; Steinbach et al., 2018; Wang et al., 2019; Lin et al., 2021). The second option is challenged by the dependency of the effective thermal conductivity on water saturation, so a proper design of the layers adjacent to the cathode CL (e.g., the cathode MPL) may be necessary. Solutions to improve water management by a modification of the cathode CL microstructure can be achieved through a tailored addition of PTFE to decrease hydrophilicity from the interior to the exterior of nanopores (see **Figure 4**). The generated Laplace pressure difference between cathode and anode can be used to push water toward the ionomer, water menisci pinned at PTFE edges to enhance evaporation (a similar approach to that used in PTFE membranes in separation processes (Lu et al., 2017; Wang et al., 2020b)), and the external hydrophobic surface outside nanopores to facilitate the transport of liquid water to the cathode MPL. A tapered geometry with a narrow tip at the PTFE surface could also be incorporated to increase the Laplace pressure difference and enhance water transport to ionomer (i.e., anode side)—a rather similar mechanism to that used by some varieties of cactus for water harvesting Malik et al. (2016). Given the variety of possibilities to improve water management, two-phase transport modeling was omitted here. The scope of this work is restricted to examining the technological limits of cathode CLs with optimal transport routes and extracting good design practices for improved performance. No flooding in the cathode CL is assumed due to cell operation at high temperature ( $T = 80^\circ\text{C}$ ) and/or the incorporation of other strategies for water management. The cathode CL is partially saturated with a representative saturation,  $s^{avg} \approx 0.4$ , including an interfacial resistance caused by water films at the entrance of nanopores.

## 2.2 Multiscale approach

A multiscale across-the-membrane model is considered to describe oxygen, proton and electron transport in the idealized bi-functional cathode CL (Mu et al., 2022). As shown in Figure 5, the representative elementary area (REA) in the CL is composed of a square region of length  $L$  and thickness  $\delta_{cl}$  with a central ionomer pillar of radius  $R_i$ . The average half-size of the secondary pore space surrounding an ionomer pillar is  $R_v$ . The ionomer pillar is covered by a nanoporous electron-conductive shell (see close-up view in Figures 5A,B). The microscopic representative elementary volume (REV) inside a shell is composed of a straight nanopore of radius  $R_p$  and length  $L_p \ll R_i$  (negligible curvature), which is catalyzed with a Pt skin of thickness  $\delta_{pt}$ . The nanoporosity of the shell is  $\varepsilon_p$  with an average spacing between pores  $l_p$  (hexagonal packing). The effect of the multicomponent microstructure and the nanoscale current generation rate are plugged into a volume-average formulation across the CL thickness by means of: 1) effective transport properties (effective diffusivity, and effective electrical and ionic conductivities), and 2) a volume-specific reaction rate (see the macro-homogeneous domain in Figure 5C). The information extracted before and during a simulation from the macroscopic REA and the microscopic REV is as follows:

- 1) Before a simulation, the bulk effective transport properties in the CL are expressed in terms of primary geometrical parameters. In the idealized geometry, the normalized dry effective molecular diffusivity,  $D_{O_2, \text{mol}}^{\text{eff, dry}} D_{O_2}^{-1}$ , is equal to the porosity of the secondary pore space,  $\varepsilon$ , to account for the reduction of the transport area with respect to the cell geometric area. The Knudsen effect, as presented before in Section 2.1, is introduced as a modification to  $D_{O_2, \text{mol}}^{\text{eff, dry}} D_{O_2}^{-1}$ . Similarly, the normalized effective ionic conductivity,  $\sigma_p^{\text{eff}} \sigma_p^{-1}$ , is given by the ionomer volume fraction,  $\varepsilon_i$ . The normalized effective electrical conductivity,  $\sigma_e^{\text{eff}} \sigma_e^{-1}$ , is modeled according to the expression for a conductive matrix embedded in a hexagonal array of non-conductive cylinders (i.e., nanopores). A hexagonal packing of nanopores provides an optimal solution to maximize the effective electrical conductivity at a given nanoporosity (Perrins et al., 1979; Tomadakis and Sotirchos, 1993). The oxygen diffusivity and the ionic conductivity in liquid water inside nanopores are  $D_{O_2, w}$  and  $\sigma_{p, w}$ , respectively. These values are corrected by the nanoporosity of the shell,  $\varepsilon_p$ , to obtain the corresponding effective values,  $D_{O_2, p}^{\text{eff}}$  and  $\sigma_{p, p}^{\text{eff}}$ . The decrease of the oxygen concentration caused by oxygen dissolution in liquid water is taken into account through Henry's constant,  $k_{H, O_2, w}$ , while the effect of the local curvature of the flux from the secondary pore space to each nanopore of radius  $R_p$  is modeled through the entry transport resistance derived by Newman (Newman, 1966).

- 2) During a simulation, oxygen and proton transport are solved in a single pore using a 1D along-the-pore model that includes a surface reaction term. The current density generated in a single pore per unit of platinized area,  $I_p$ , is determined, and then converted into a local volumetric current density,  $j_c(y)$ , through the roughness factor,  $r_f$ . The inlet boundary conditions for oxygen and protons in the microscopic model are provided by the local solution of the macroscopic model at each spatial coordinate across the thickness,  $y$ -coordinate. The local electronic potential,  $\phi_e(y)$ , used to evaluate the local overpotential,  $\eta_c(y)$ , is also provided by the macroscopic model.

The oxygen diffusive resistance from the channel to the CL and the ohmic resistance of the PEM and its interfaces are incorporated through integral mixed boundary conditions into the 1D cathode CL model. Further details of the implementation can be found in (Sánchez-Ramos et al., 2021). The formulations of the macroscopic and microscopic models are presented in the next two sections.

## 3 Macroscopic model (layer scale)

The macroscopic conservation equations of oxygen, protons and electrons across the CL thickness ( $y$ -coordinate) are given by

$$\frac{d}{dy} \left( -D_{O_2}^{\text{eff}} \frac{dC_{O_2}}{dy} \right) = -\frac{j_c}{4F} \quad (8a)$$

$$\frac{d}{dy} \left( -\sigma_p^{\text{eff}} \frac{d\phi_p}{dy} \right) = -j_c \quad (8b)$$

$$\frac{d}{dy} \left( \sigma_e^{\text{eff}} \frac{d\phi_e}{dy} \right) = -j_c \quad (8c)$$

where  $D_{O_2}^{\text{eff}}$ ,  $\sigma_p^{\text{eff}}$  and  $\sigma_e^{\text{eff}}$  are the effective oxygen diffusivity, ionic conductivity and electronic conductivity in the bulk CL, respectively, and  $j_c$  is the volumetric current density (the negative sign accounts for consumption, i.e.,  $j_c > 0$ ).

### 3.1 Boundary conditions

Equations (8a)–(8c) are supplemented with the following boundary conditions at the CL/MPL ( $y = \delta_{cl}$ ) and CL/PEM ( $y = 0$ ) interfaces (see Figure 5).

$$C_{O_2} \Rightarrow \text{CL/MPL: } C_{O_2} = C_{O_2, cl}^{\text{in}}; \quad \text{CL/PEM: } \frac{dC_{O_2}}{dy} = 0 \quad (9a)$$

$$\phi_p \Rightarrow \text{CL/MPL: } \frac{d\phi_p}{dy} = 0; \quad \text{CL/PEM: } \phi_p = -\Delta\phi_p \quad (9b)$$

$$\phi_e \Rightarrow \text{CL/MPL: } \phi_e = V_{\text{cell}}; \quad \text{CL/PEM: } \frac{d\phi_e}{dy} = 0 \quad (9c)$$

where  $V_{\text{cell}}$  is the operating cell voltage,  $C_{\text{O}_2}^{\text{in}}$  is the inlet oxygen concentration at the MPL/CL interface, and  $\Delta\phi_p$  is the ionic potential drop across the PEM (and its interfaces). The last two quantities are related with the output current density,  $I^{\text{avg}}$ , through the following expressions.

$$C_{\text{O}_2, \text{cl}}^{\text{in}} = C_{\text{O}_2, \text{ch}}^{\text{in}} - R_{\text{O}_2}^{\text{chl}} \frac{I^{\text{avg}}}{4F} \quad (10a)$$

$$\Delta\phi_p = \text{ASR}_{\text{pem}} I^{\text{avg}} \quad (10b)$$

where  $R_{\text{O}_2}^{\text{chl}}$  is the oxygen transport resistance from the channel to the MPL/CL interface,  $\text{ASR}_{\text{pem}}$  is the area-specific ionic resistance of the PEM, and  $C_{\text{O}_2, \text{ch}}^{\text{in}}$  is the channel oxygen concentration. The output current density is given by

$$I^{\text{avg}} = \int_0^{\delta_{\text{cl}}} j_c(y) dy \quad (11)$$

According to the ideal gas law, the oxygen concentration in the air feed channel depends on the inlet cathode pressure,  $p_{\text{g}, \text{c}}^{\text{in}}$ , and relative humidity,  $\text{RH}_{\text{c}}$ , as

$$C_{\text{O}_2, \text{ch}}^{\text{in}} = \frac{p_{\text{O}_2}^{\text{in}}}{R^0 T}; \quad p_{\text{O}_2}^{\text{in}} = 0.21 (p_{\text{g}, \text{c}}^{\text{in}} - \text{RH}_{\text{c}} p_{\text{H}_2\text{O}}^{\text{sat}}) \quad (12)$$

### 3.2 Constitutive equations of the porous medium

Considering the representative geometry shown in **Figure 5**, the porosity of the secondary pore space,  $\varepsilon$ , the ionomer volume fraction,  $\varepsilon_i$ , the volume fraction of electron-conductive solid and Pt,  $\varepsilon_{\text{c+Pt}}$ , and the porosity of the primary pore space,  $\varepsilon_{\text{prim}}$ , are equal to.

$$\varepsilon \left( \tilde{R}_i, \frac{L_p}{L} \right) = 1 - \pi \left( \tilde{R}_i + \frac{L_p}{L} \right)^2 \quad (13a)$$

$$\varepsilon_i(\tilde{R}_i) = \pi \tilde{R}_i^2 \quad (13b)$$

$$\varepsilon_{\text{c+Pt}} \left( \tilde{R}_i, \frac{L_p}{L}, \varepsilon_p \right) = \pi \left[ \left( \tilde{R}_i + \frac{L_p}{L} \right)^2 - \tilde{R}_i^2 \right] (1 - \varepsilon_p) \quad (13c)$$

$$\varepsilon_{\text{prim}} \left( \tilde{R}_i, \frac{L_p}{L}, \varepsilon_p \right) = \pi \left[ \left( \tilde{R}_i + \frac{L_p}{L} \right)^2 - \tilde{R}_i^2 \right] \varepsilon_p \quad (13d)$$

where the ionomer radius ratio is equal to  $\tilde{R}_i = R_i/L$ . It can be verified that  $\varepsilon + \varepsilon_i + \varepsilon_{\text{c+Pt}} + \varepsilon_{\text{prim}} = 1$ .

The characteristic half-size of the secondary pore space,  $R_v$ , and the spacing between nanopores in the electron-conductive shell,  $l_p$ , are given by.

$$\frac{R_v}{L} \left( \tilde{R}_i, \frac{L_p}{L} \right) = \sqrt{1 - \pi \left( \tilde{R}_i + \frac{L_p}{L} \right)^2} \quad (14a)$$

$$\frac{l_p}{R_p} (\varepsilon_p) = \sqrt{\frac{2\pi}{\varepsilon_p}} \quad (\text{hexagonal packing}) \quad (14b)$$

Ideally, all nanopores are accessible and lined with active Pt. Hence, the roughness factor,  $r_f$ , and the catalyst specific surface area,  $a_{\text{Pt}}$ , are equal to.

$$r_f = \frac{2\pi N_p R_p L_p}{L^2} = \frac{L_{\text{Pt}}}{\delta_{\text{Pt}} \rho_{\text{Pt}}} \quad (15a)$$

$$a_{\text{Pt}} R_p \left( \tilde{R}_i, \frac{L_p}{L}, \varepsilon_p \right) = r_f \frac{R_p}{\delta_{\text{cl}}} = 2\pi \varepsilon_p \left[ \left( \tilde{R}_i + \frac{L_p}{L} \right)^2 - \tilde{R}_i^2 \right] \quad (15b)$$

where  $N_p$  is the number of pores in a conductive shell. For a prescribed nanoporosity,  $N_p$  is given by

$$\varepsilon_p = \frac{N_p \pi R_p^2 L_p}{\pi \left[ \left( R_i + L_p \right)^2 - R_i^2 \right] \delta_{\text{cl}}} \Rightarrow N_p = \frac{\varepsilon_p \delta_{\text{cl}} \left[ \left( R_i + L_p \right)^2 - R_i^2 \right]}{R_p^2 L_p} \quad (16)$$

The CL thickness,  $\delta_{\text{cl}}$ , is determined by the Pt loading,  $L_{\text{Pt}}$ , i.e.,

$$\begin{aligned} L_{\text{Pt}} &= \frac{r_f}{\text{ECSA}} = r_f \delta_{\text{Pt}} \rho_{\text{Pt}} \Rightarrow \frac{\delta_{\text{cl}}}{R_p} \left( \tilde{R}_i, \frac{L_p}{L}, \varepsilon_p \right) \\ &= \frac{L_{\text{Pt}}}{2\pi \varepsilon_p \delta_{\text{Pt}} \rho_{\text{Pt}} \left[ \left( \tilde{R}_i + \frac{L_p}{L} \right)^2 - \tilde{R}_i^2 \right]} \end{aligned} \quad (17)$$

Here,  $\rho_{\text{Pt}} = 21,450 \text{ kg m}^{-3}$  is the density of Pt. Note that the ECSA =  $L_{\text{Pt}} (\delta_{\text{Pt}} \rho_{\text{Pt}})^{-1}$  is directly related to the thinness of the Pt skin. For a Pt atomic layer,  $\delta_{\text{Pt}} \approx 0.2 \text{ nm}$ , we yield ECSA  $\approx 230 \text{ m}^2 \text{ g}_{\text{Pt}}^{-1}$  (Xie et al., 2014). The roughness factor is fixed for a given Pt loading and thickness of Pt skin.

### 3.3 Effective transport properties

The expressions of the bulk effective transport properties at the layer scale are presented below.

#### 3.3.1 Effective oxygen diffusivity

The effective oxygen diffusivity is decomposed into a dry component due to the obstruction of the dry CL microstructure and the Knudsen effect,  $f(\varepsilon, R_v)$ , and the relative effective diffusivity due to the relative blockage of water saturation,  $g(s^{\text{avg}})$

(Sánchez-Ramos et al., 2021; García-Salaberri et al., 2015b,a; García-Salaberri, 2021)

$$\frac{D_{O_2}^{\text{eff}}}{D_{O_2}^{\text{mol}}} = \frac{D_{O_2}^{\text{eff,dry}}}{D_{O_2}^{\text{mol}}} \frac{D_{O_2}^{\text{eff}}}{D_{O_2}^{\text{eff,dry}}} \quad (18)$$

$$\frac{D_{O_2}^{\text{eff}}}{D_{O_2}^{\text{mol}}} = \frac{D_{O_2}^{\text{eff,dry}}}{\frac{f(\varepsilon, R_p)}{g(s^{\text{avg}})}} \frac{D_{O_2}^{\text{eff}}}{D_{O_2}^{\text{eff,dry}}}$$

where  $D_{O_2}^{\text{mol}}(p_{g,c}, T)$  is the molecular diffusivity of oxygen in air (Ye and Van Nguyen, 2007)

$$D_{O_2}^{\text{mol}} = 2.65 \times 10^{-5} \left( \frac{T}{333} \right)^{1.5} \left( \frac{10^5}{p_{g,c}} \right) \quad [\text{m}^2 \text{s}^{-1}] \quad (19)$$

with  $T$  expressed in K and  $p_{g,c}$  in Pa.

For a tortuosity factor  $\tau \approx 1$ , the normalized dry effective diffusivity is equal to

$$f(\varepsilon, R_p) = \varepsilon \left( 1 + \frac{D_{O_2}^{\text{mol}}}{D_{O_2}^{\text{knud}}} \right)^{-1} \quad (20)$$

where  $D_{O_2}^{\text{knud}}$  is the Knudsen diffusivity given by Eq. 3 with  $R = R_p$  and  $i = O_2$ .

According to the data collected in Sánchez-Ramos et al. (2021),  $g(s^{\text{avg}})$  in conventional CLs can be modeled as a power law of the form

$$g(s^{\text{avg}}) = (1 - s^{\text{avg}})^{2.5} \quad (21)$$

This expression was considered a reasonable first approximation to evaluate  $g(s^{\text{avg}})$  in this work.

### 3.3.2 Effective proton conductivity

Proton conduction through hydrated ionomer pillars also features a tortuosity factor  $\tau \approx 1$ . Hence, we have that

$$\frac{\sigma_p^{\text{eff}}}{\sigma_p} = \varepsilon_i \quad (22)$$

where  $\sigma_p$  is the bulk proton conductivity in ionomer. The value of  $\sigma_p$  in finite-sized ionomer domains depends on the size of the conductive medium and the confined morphology of protogenic groups (thin film vs. nanofiber). 2D thin ionomer films in conventional CLs show a lower conductivity than bulk PEMs (2-10 times lower) due to the more difficult percolation of protons through finite thickness domains (Siroma et al., 2009; Paul et al., 2014; Gostick and Weber, 2015; Chen et al., 2019), increasing with the film thickness—the bulk value of PEMs is reached when the film thickness is significantly larger than the size of protogenic nanodomains (around 10 nm) (Gomaa et al., 2022). However, ionomer nanofibers show an opposite behavior, reaching a higher ionic conductivity for small fiber diameters compared with bulk PEMs (up to 10 times higher) and a similar ionic conductivity to that of PEMs for significantly high fiber diameters (Pan et al., 2008; Sun et al., 2019). This opposite behavior can be explained by

the preferential alignment of protogenic nanodomains along nanofibers, which act as highways for proton conduction (Pan et al., 2008). Thin films and nanofibers reach a value comparable to that of bulk PEMs for thicknesses and diameters around 50–100 nm, which is similar to the mean diameter of ionomer pillars considered here. Therefore, the bulk proton conductivity at fully humidified conditions was assumed equal to that of Nafion PEMs as a first approximation (Kusoglu and Weber, 2017)

$$\sigma_p \approx 10 \text{ S m}^{-1} \quad (23)$$

### 3.3.3 Effective electrical conductivity

The effective electrical conductivity in the electron-conductive shell with a hexagonal packing of nanopores,  $\sigma_{e,sh}^{\text{eff}}$ , is modeled by the low-order analytical solution of Perrins et al. (Perrins et al., 1979)

$$\frac{\sigma_{e,sh}^{\text{eff}}}{\sigma_e} = 1 - \frac{2\varepsilon_p}{1 + \varepsilon_p - \frac{0.075422 \varepsilon_p^6}{1 - 1.060283 \varepsilon_p^{12}} - 0.000076 \varepsilon_p^{12}} \quad (24)$$

where  $\sigma_e$  is the bulk electrical conductivity of the electron-conductive material. Here, the electrical conductivity of graphite was taken as a representative value,  $\sigma_e \sim 10^6 \text{ S m}^{-1}$ . A material with a high stiffness would also be necessary to provide mechanical integrity to the proposed core-shell microstructure for its fabrication.

At the layer scale,  $\sigma_{e,sh}^{\text{eff}}$  is corrected by the volume fraction of the conductive shell,  $\varepsilon_{sh}$ , to account for the reduced area available for transport

$$\sigma_e^{\text{eff}} = \varepsilon_{sh} \sigma_{e,sh}^{\text{eff}}, \quad \varepsilon_{sh} = \frac{\varepsilon_{c+Pt}}{1 - \varepsilon_p} \quad (25)$$

## 4 Microscopic model (nanopore scale)

Oxygen and proton transport along a nanopore (local  $x$ -coordinate) is governed by a reaction-diffusion equation with a surface reactive term. Mass and charge balances in a pore segment of length  $dx$  and radius  $R_p$  yield.

$$\pi R_p^2 \frac{d}{dx} \left( -D_{O_2,p}^{\text{eff}} \frac{dC_{O_2,p}}{dx} \right) dx = -2\pi R_p dx \frac{I_p(x)}{4F} \quad (26a)$$

$$\pi R_p^2 \frac{d}{dx} \left( -\sigma_{p,p}^{\text{eff}} \frac{d\phi_{p,p}}{dx} \right) dx = -2\pi R_p dx I_p(x) \quad (26b)$$

The resulting differential conservation equations for the nanoscale oxygen concentration,  $C_{O_2,p}$ , and the ionic potential,  $\phi_{p,p}$ , are

$$\frac{d}{dx} \left( -D_{O_2,p}^{\text{eff}} \frac{dC_{O_2,p}}{dx} \right) = -\frac{2}{R_p} \frac{I_p(x)}{4F} \quad (27a)$$

$$\frac{d}{dx} \left( -\sigma_{p,p}^{\text{eff}} \frac{d\phi_{p,p}}{dx} \right) = -\frac{2}{R_p} I_p(x) \quad (27b)$$

where  $I_p(x)$  is the current density generated in a single nanopore per unit of active surface area (i.e., internal nanopore surface).  $I_p(x)$  is described by Tafel kinetics (Sánchez-Ramos et al., 2018)

$$I_p(x) = i_{o,c} \left( \frac{C_{O_2,p}}{C_{O_2}^{\text{ref}}} \right)^{\gamma} \exp \left[ -\frac{\alpha_c F}{R^{\circ} T} \eta_c(x) \right] \quad (28)$$

Here,  $i_{o,c} \approx 0.5 \text{ A m}_{\text{Pt}}^{-2}$  is the exchange current density,  $\gamma = 0.7$  the reaction order,  $\alpha_c = 0.5$  the symmetry coefficient,  $C_{O_2}^{\text{ref}} \approx 40 \text{ mol m}^{-3}$  the reference oxygen concentration, and  $\eta_c$  the cathode overpotential.  $i_{o,c}$  was set somewhat higher than the mean value reported in (Sánchez-Ramos et al., 2021) ( $0.5 \text{ A m}_{\text{Pt}}^{-2}$  vs.  $0.3 \text{ A m}_{\text{Pt}}^{-2}$  at  $T = 80^{\circ}\text{C}$ ) due to improved catalyst activity in ultra-thin Pt skins not covered by ionomer ( $\delta_{\text{Pt}} \leq 1 \text{ nm}$ ) (Debe, 2012; Xie et al., 2014; Yarlagadda et al., 2018). The cathode overpotential ( $\eta_c \leq 0$ ) is defined as

$$\eta_c(x, y) = \phi_e(y) - \phi_{p,p}(x) - E_r \quad (29)$$

where  $\phi_e(y)$  is the local electronic potential across the thickness (provided by the layer-scale model) and  $E_r \approx 1.2 \text{ V}$  is the reversible cell voltage (Sánchez-Ramos et al., 2021).

The effective oxygen diffusivity,  $D_{O_2,p}^{\text{eff}}$ , and the effective ionic conductivity,  $\sigma_{p,p}^{\text{eff}}$ , in a water-filled nanopore are equal to

$$D_{O_2,p}^{\text{eff}} = \varepsilon_p D_{O_2,w}; \quad \sigma_{p,p}^{\text{eff}} = \varepsilon_p \sigma_{p,w} \quad (30)$$

where  $D_{O_2,w}$  and  $\sigma_{p,w}$  are the diffusivity coefficient of oxygen and the proton conductivity in liquid water, respectively.  $D_{O_2,w}$  can be extracted from values measured in bulk water (Han and Bartels, 1996; Muzaffar et al., 2018), while  $\sigma_{p,w}$  has been determined experimentally and numerically for pH values commonly found in operating PEMFCs (see (Zenyuk and Litster, 2014; Liu and Zenyuk, 2018) and references therein)

$$D_{O_2,w} \approx 5 \times 10^{-9} \text{ m}^2 \text{ s}^{-1}; \quad \sigma_{p,w} \approx 10^{-1} \text{ S m}^{-1} \quad (31)$$

Comparatively,  $D_{O_2,w}$  is between one to three orders of magnitude higher than the oxygen diffusivity in ionomer films and PEMs (Kusoglu and Weber, 2017; Sánchez-Ramos et al., 2021), while  $\sigma_{p,w}$  is one order of magnitude lower than the proton conductivity through thin films in conventional CLs (Sabarirajan et al., 2020). This favorable situation was

previously exploited in NSTFC electrodes with a relatively good performance (Debe et al., 2011; Debe, 2012).

At each  $y$ -coordinate, the surface current density drawn from one nanopore is equal to

$$I_p^{\text{avg}}(y) = \frac{1}{L_p} \int_0^{L_p} I_p(x) dx \quad (32)$$

The relationship between the nanoscale surface current density,  $I_p^{\text{avg}}$ , and the local volumetric current density at the layer scale,  $j_c(y)$ , is given by the active specific surface area (see Eq. 15b)

$$j_c(y) = I_p^{\text{avg}}(y) a_{\text{Pt}} \quad (33)$$

## 4.1 Boundary conditions

The boundary conditions at the nanopore inlet ( $x = L_p$ ) and at the nanopore/ionomer interface ( $x = 0$ ) are rather similar to those used at the layer scale due to the analogy between the arrangement of a nanopore inside the idealized bi-functional CL and a CL in a MEA

$$\begin{aligned} C_{O_2,p} \Rightarrow \text{Inlet: } C_{O_2} &= C_{O_2,p}^{\text{in}}(y) - D_{O_2,p}^{\text{eff}} \frac{dC_{O_2,p}}{dx} R_{O_2,p}^{\text{in}}; \\ \text{Ionomer: } \frac{dC_{O_2,p}}{dy} &= 0 \end{aligned} \quad (34a)$$

$$\phi_{p,p} \Rightarrow \text{Inlet: } \frac{d\phi_{p,p}}{dy} = 0; \quad \text{Ionomer: } \phi_{p,p} = \phi_p(y) + \sigma_{p,p}^{\text{eff}} \frac{d\phi_{p,p}}{dx} R_{p,p}^{\text{in}} \quad (34b)$$

where the dissolved oxygen concentration in liquid water at the nanopore inlet is given by Henry's law (Blunier et al., 2013) (rather than a Langmuir adsorption model as found for ionomers (Shen et al., 2017; Cheng et al., 2022))

$$C_{O_2,p}^{\text{in}}(y) = k_{\text{H},O_2,w} C_{O_2}(y); \quad \frac{R^{\circ} T}{k_{\text{H},O_2,w}} = 7.79 \times 10^4 \exp \left( 5.7 - \frac{1700}{T} \right) \quad (35)$$

The entry resistances at the nanopore edges,  $R_{O_2,p}^{\text{in}}$  and  $R_{p,p}^{\text{in}}$ , can be expressed as Newman (1966)

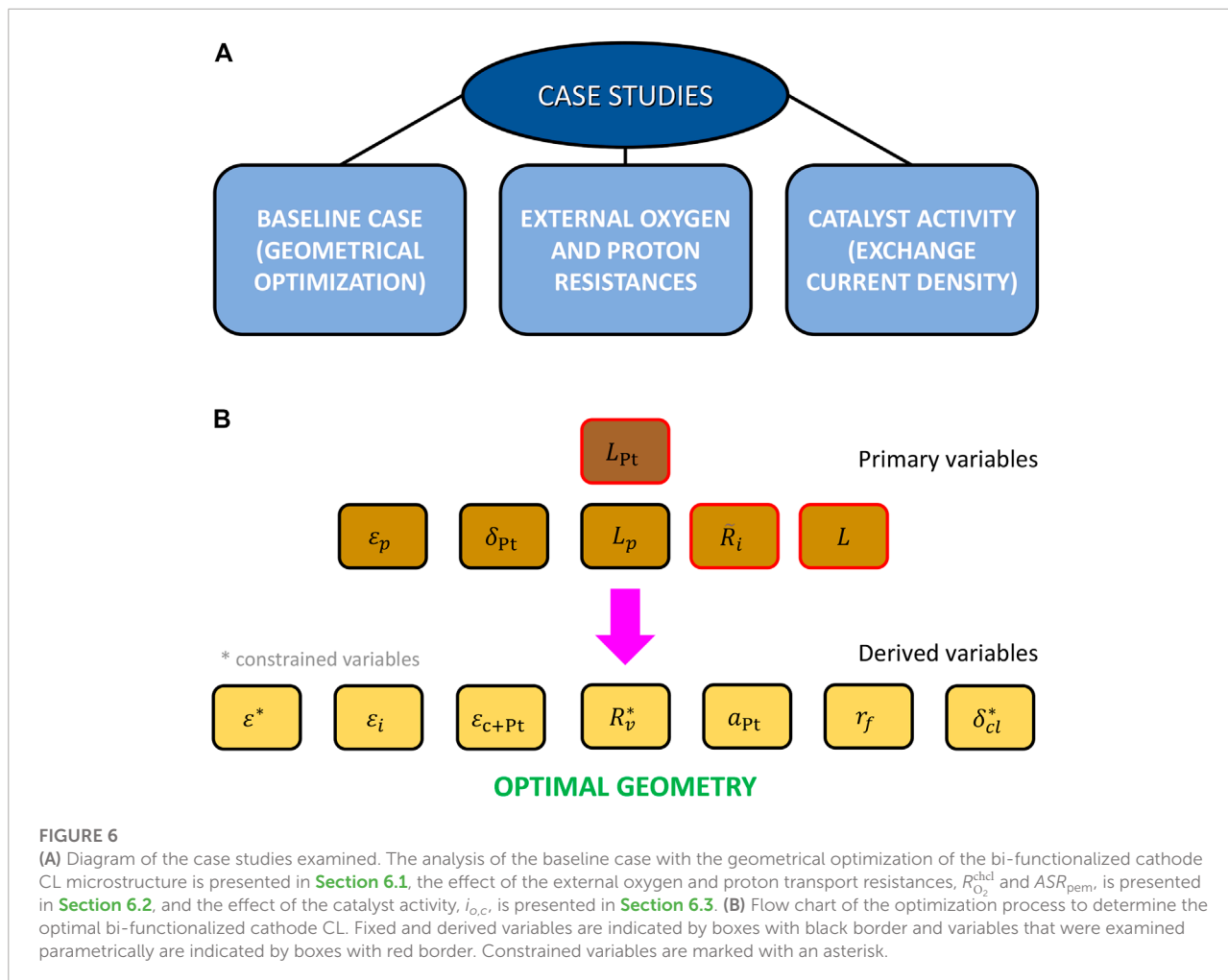
$$R_{O_2}^{\text{in}} = \frac{\pi R_p}{4D_{O_2,w}}; \quad R_p^{\text{in}} = \frac{\pi R_p}{4\sigma_{p,w}}, \quad (36)$$

leading to robin boundary conditions.

## 5 Case studies

The three case studies examined are schematized in Figure 6A: 1) baseline case devoted to the geometrical optimization of the CL microstructure (see optimization flow chart in Figure 6B) considering state-of-the-art channel-CL oxygen transport and area-specific ohmic resistances,





$R_{O_2}^{chd} = 1 \text{ s cm}^{-1}$  and  $ASR_{pem} = 0.02 \text{ cm}^2 \text{ S}^{-1}$ , respectively (see, e.g. ([Owejan et al., 2013, 2014](#); [Ureña et al., 2021](#); [Gomaa et al., 2022](#))); 2) an analysis of the exterior mass and proton transport resistances,  $R_{O_2}^{chd}$  and  $ASR_{pem}$ , where the baseline values are reduced to  $R_{O_2}^{chd} = 0.5 - 0.1 \text{ s cm}^{-1}$  and  $ASR_{pem} = 0.01 - 0.002 \text{ cm}^2 \text{ S}^{-1}$  (x0.5 and x0.1); 3) an analysis of the catalyst activity, i.e., the exchange current density,  $i_{o,c}$ , where the baseline value  $i_{o,c} = 0.5 \text{ A m}_{Pt}^{-2}$  is increased up to  $i_{o,c} = 1 - 5 \text{ A m}_{Pt}^{-2}$  (x2 and x10).

The parameters that were kept constant and examined parametrically for the geometrical optimization (presented in [Section 6.1](#)) are listed in [Table 1](#). The nanopore radius was fixed to  $R_p = 2.5 \text{ nm}$  to ensure the presence of water in tiny nanopores and the average saturation in the secondary pore space was fixed to  $s^{avg} = 0.4$ , as previously discussed in [Section 2.1](#). The cell voltage was set to  $V_{cell} = 0.5 \text{ V}$ , close to maximum power density (see footnote in [Table 1](#) for other operating conditions). The Pt loading was varied in the range  $L_{Pt} = 0.001 - 0.4 \text{ mg}_{Pt} \text{ cm}^{-2}$ , which includes the loading needed to meet the ultimate target of a total PGM content below

$0.1 \text{ mg}_{Pt} \text{ cm}^{-2}$  ( $L_{Pt} \sim 10^{-2} \text{ mg}_{Pt} \text{ cm}^{-2}$ ). For a given Pt loading, the CL microstructure is defined by five primary variables:  $\epsilon_p$ ,  $\delta_{Pt}$ ,  $L_p$ ,  $L$  and  $\bar{R}_i$ . The nanoporosity of the shell was kept as high as possible,  $\epsilon_p = 0.9$ , below the percolation threshold given by  $\epsilon_p^{max} = 1 - \pi/(2\sqrt{3}) \approx 0.906$ , the thickness of the Pt skin was set to  $\delta_{Pt} = 0.2 \text{ nm}$  to maximize the ECSA and the nanopore length was fixed to  $L_p = 10 \text{ nm}$  to minimize the transport length in nanopores, while providing certain mechanical integrity. The ionomer radius ratio was varied between  $\bar{R}_i = 0.1 - 0.4$  and the spacing between pillars between  $L = L^{min} - 5000 \text{ nm}$ , where  $L^{min}$  is the minimum spacing allowed to ensure a minimum half-size and porosity of the secondary pore space (see below). The remaining variables ( $\epsilon$ ,  $\epsilon_i$ ,  $\epsilon_{c+Pt}$ ,  $R_v$ ,  $r_f$ ,  $a_{Pt}$  and  $\delta_{cl}$ ) can be derived from the constitutive equations of the porous medium presented in [Section 3.2](#). The volume fractions ( $\epsilon$ ,  $\epsilon_i$ ,  $\epsilon_{c+Pt}$ ) can be determined from [Eqs. \(13a\)–\(13c\)](#), the half-size of the secondary pore space ( $R_v$ ) from [Eq. 14a](#), the roughness factor and the specific surface area ( $r_f$ ,  $a_{Pt}$ ) from [Eqs. \(15a\)–\(15b\)](#), and the CL thickness from [Eq. 17](#). In addition, three geometrical constraints were imposed on the above variables: (1-2)  $\epsilon \geq 0.15$  and  $R_v \geq 0$

TABLE 1 Model parameters. The baseline case corresponds to  $R_{O_2}^{chl} = 1 \text{ s cm}^{-1}$ ,  $ASR_{pem} = 0.02 \text{ cm}^2 \text{ S}^{-1}$  and  $i_{o,c} = 0.5 \text{ A m}_{Pt}^{-2}$ . The constrained variables are indicated with an asterisk and the operating conditions are included in the footnote.

Parameter	Symbol	Value
Channel-CL $O_2$ transport resistance	$R_{O_2}^{chl}$	0.1, 0.5, 1 (baseline) $\text{s cm}^{-1}$
Area-specific ohmic resistance (~ PEM)	$ASR_{pem}$	0.002, 0.01, 0.02 (baseline) $\text{cm}^2 \text{ S}^{-1}$
Exchange current density	$i_{o,c}$	0.5 (baseline), 1, 5 $\text{A m}_{Pt}^{-2}$
Pt skin thickness (~ atomic layer)	$\delta_{Pt}$	0.2 nm
Nanopore radius	$R_p$	2.5 nm
Nanopore length	$L_p$	10 nm
Shell nanoporosity	$\epsilon_p$	0.9
Average water saturation	$s^{avg}$	0.4
Pt loading	$L_{Pt}$	0.001–0.3 $\text{mg}_{Pt} \text{ cm}^{-2}$
Pillar spacing	$L$	$L^{\min} - 5000 \text{ nm}$
Ionomer radius ratio	$\tilde{R}_i$	0.1–0.4
Porosity of secondary pore space*	$\epsilon$	$\geq 0.15$
Half-size of secondary pore space*	$R_v$	$\geq 0$
CL thickness*	$\delta_{cl}$	$\geq 1.5 \text{ }\mu\text{m}$

$P_{g,e} = 1.5 \text{ bar}$ ;  $P_{g,a} = 1 \text{ bar}$ ;  $T = 80^\circ\text{C}$ ;  $RH_a = RH_c = 1$ ;  $C_{O_2,cl}^{in} = 7.4 \text{ mol m}^{-3}$ ;  $V_{cell} = 0.5 \text{ V}$ .

to avoid an exceedingly low bulk oxygen effective diffusivity, and 3)  $\delta_{cl} \geq 1.5 \text{ }\mu\text{m}$  to ensure a minimum mechanical integrity of the porous layer and avoid edge effects, such as capillary condensation at sharp angles (Mashio et al., 2014). The lower threshold used here for the thickness is similar to that considered in previous works with conventional CLs (Sun et al., 2020). The lowest pillar spacing imposed by constraints 1–2,  $L_\epsilon^{\min}$  and  $L_{R_v}^{\min}$ , can be determined from Eq. 13a, Eq. 14a, leading to

$$L_\epsilon^{\min} = \frac{L_p}{\sqrt{\frac{1 - \epsilon^{\min}}{\pi} - \tilde{R}_i}} \quad (37a)$$

$$L_{R_v}^{\min} = \frac{L_p}{1 - \tilde{R}_i} \quad (37b)$$

Therefore, the smallest pillar spacing allowed is equal to  $L^{\min} = \max\{L_\epsilon^{\min}, L_{R_v}^{\min}\}$ .

## 6 Discussion of results

### 6.1 Baseline case (geometrical optimization)

The calculation of the optimal pillar spacing and ionomer radius ratio,  $L$  and  $\tilde{R}$ , was accomplished using physical considerations rather than a purely mathematical approach. Eqs. (27a)–(27b) are governed by two dimensionless parameters, which arise from the ratios of the characteristic times of oxygen and proton transport and the characteristic reaction time at both the nanoscale ( $\Omega_{O_2}^p$ ,  $\Omega_p^p$ ) and the layer scale ( $\Omega_{O_2}^{cl}$ ,  $\Omega_p^{cl}$ ) (Sánchez-Ramos et al., 2022). An alternative interpretation can be considered as the ratios of the diffusion/conduction

penetration depths and the characteristic length at a certain scale (Perry et al., 1998; Kulikovskiy, 2010). For a roughness factor in the range  $r_f \sim 1$ –100 and a representative average current density needed for high performance,  $I^{avg} \sim 2 \text{ A cm}^{-2}$ , we yield the following estimations.

$$\Omega_{O_2}^p = \frac{t_{d,p}}{t_{r,p}} = \frac{L_p}{l_{O_2,p}} \sim \frac{L_p R_{O_2}^p I^{avg}}{C_{O_2,p}^{in} R_p r_f} \sim 10^{-1} (r_f \sim 10^2) - 1 (r_f \sim 1) \propto r_f^{-1} \text{ (limiting at low } L_{Pt}) \quad (38a)$$

$$\Omega_{O_2}^{cl} = \frac{t_{d,cl}}{t_r} = \frac{\delta_{cl}}{l_{O_2,cl}} \sim \frac{R_{O_2}^{cl} I^{avg}}{C_{O_2,cl}^{in} F} \sim 10^{-2} - 10^{-1} \quad r_f\text{-independent} \quad (38b)$$

$$\Omega_p^p = \frac{t_{d,p} t_{p,p}}{t_{r,p} t_{d,p}} = \frac{L_p}{l_{p,p}} \sim \frac{ASR_p^p L_p I^{avg}}{E_r R_p r_f} \sim 10^{-4} (r_f \sim 10^2) - 10^{-2} (r_f \sim 1) \propto r_f^{-1} \quad (38c)$$

$$\Omega_p^{cl} = \frac{t_{d,cl} t_{p,cl}}{t_r t_{d,cl}} = \frac{\delta_{cl}}{l_{p,cl}} \sim \frac{ASR_p^{cl} I^{avg}}{E_r} \sim 10^{-3} - 10^{-2} \quad r_f\text{-independent} \quad (38d)$$

where the oxygen transport resistances at the layer scale and the nanoscale (under passive non-reactive conditions) are equal to  $R_{O_2}^{cl} = \delta_{cl}/D_{O_2}^{eff}$  and  $R_{O_2}^p = L_p/D_{O_2,p}^{eff}$ , respectively, and the proton transport resistances at the layer scale and the nanoscale are equal to  $ASR_p^{cl} = \delta_{cl}/\sigma_p^{eff}$  and  $ASR_p^p = L_p/\sigma_{p,p}^{eff}$ , respectively. (Note that the apparent bulk diffusive resistance under reactive conditions is proportional to that under passive conditions (see, e.g. (Schuler et al., 2019)), so the optimization problem at the layer scale can be reduced to minimizing  $R_{O_2}^{cl}$  if other losses are not significant). The characteristic oxygen

concentration drops were estimated as  $C_{O_2,p}^{in} \sim k_{H_2O_2,w} C_{O_2,ch}^{in}$  and  $C_{O_2,cl}^{in} \sim C_{O_2,ch}^{in}$ , and the characteristic ionic potential drop as  $E_r$ . The dimensionless transport coefficients at the nanoscale depend on  $r_f$  because of the re-normalization between the cell current density and the current density per unit of active area, i.e.,  $I^{avg} = r_f I_p^{avg}$ .

The most limiting transport process is oxygen transport at the nanoscale mainly due to the larger oxygen resistance at the nanoscale (compared with that of the bulk CL) and the dissolution of oxygen in liquid water to reach triple phase points unlike proton conduction. Ohmic losses at the layer scale can be lower or comparable to those found in water-filled nanopores depending on the value of the normalized ionic conductivity across the CL ( $\sigma_p^{eff} \sigma_p^{-1} = \varepsilon_i$  in our case and dependent on bottlenecks created by thin films in conventional CLs (Sabarirajan et al., 2020)). For  $r_f \approx 1$ , regardless of  $I^{avg}$ , we yield

$$\frac{\Omega_{O_2}^p}{\Omega_{O_2}^{cl}} \sim \frac{L_p}{R_p} \times \frac{1}{k_{H_2O_2,w}} \times \frac{R_{O_2}^p}{R_{O_2}^{cl}} \sim (1-10) \times 10 \times (1-10) \sim 10-10^3 \quad (39a)$$

$$\frac{\Omega_p^p}{\Omega_p^{cl}} \sim \frac{L_p}{R_p} \times \frac{ASR_p^p}{ASR_p^{cl}} \sim (1-10) \times (10^{-1}-1) \sim 10^{-1}-10 \quad (39b)$$

The maximum power density is achieved when all the dimensionless times (or penetration depths),  $\Omega_i$ , are minimized (maximized), so that oxygen and proton transport are fast enough to maintain the reaction rate at the targeted current density,  $I^{avg}$ , with a low cathode overpotential. According to Eqs. (38a)–(38d), this condition is achieved when transport resistances,  $R_i$ , are minimized at all scales. The other option is to increase the oxygen concentration at the CL/MPL interface, something that can be done through a reduction of the exterior mass transport resistance to the cathode CL,  $R_{O_2}^{cl}$ . Increasing Henry's constant of oxygen in liquid water is difficult, even though it is worth noting that the oxygen diffusivity in liquid water can be slightly increased using oxygen diffusion-enhancing compounds (usually used in medicine for the treatment of diseases, such as hypoxia and ischemia) (Stennett et al., 2006).

Figure 7A shows the variation of the bulk oxygen transport resistance,  $R_{O_2}^{cl}$ , as a function of  $L$  for various Pt loadings ( $\tilde{R}_i = 0.3$ ). For a given Pt loading, there is a critical  $L$  for which  $R_{O_2}^{cl}$  is minimized due to a trade-off between the increasing secondary pore size (lower  $R_{O_2}^{cl}$ ) and the increasing thickness (higher  $R_{O_2}^{cl}$ ) with  $L$  (see Eq. 14a and (17)). The optimal spacing is approximately reached when  $\delta_{cl}$  is minimum,  $\delta_{cl} = \Pi \delta_{cl}^{min}$ ;  $\Pi = 1.2$  was taken here. The nearly minimum thickness also minimizes the bulk proton transport resistance,  $R_p^{cl}$ . Hence, the optimal design spacing,  $L^{des}(\tilde{R}_i)$ , can be determined from the

condition

$$\Pi \delta_{cl}^{min} = \frac{L_{Pt} R_p}{2\pi \varepsilon_p \delta_{Pt} \rho_{Pt} \left[ \left( \tilde{R}_i^{des} + \frac{L_p}{L^{des}} \right)^2 - \left( \tilde{R}_i^{des} \right)^2 \right]}; \quad \Pi = 1.2 \quad (40a)$$

And the solid volume fraction,  $\varepsilon_{c+Pt}$ , can then be calculated from

$$\varepsilon_{c+Pt}^{des} = \pi \left[ \left( \tilde{R}_i^{des} + \frac{L_p}{L^{des}} \right)^2 - \left( \tilde{R}_i^{des} \right)^2 \right] (1 - \varepsilon_p) \quad (40b)$$

As shown in Figure 7B,  $L^{des}$  increases with decreasing Pt loading, given that a smaller amount of Pt can be allocated in the same thickness but with larger secondary pores (where most of the pore space is present). This method of reducing  $L_{Pt}$  is theoretically optimal (compared with the addition of bare carbon to maintain a constant thickness), since it decreases  $R_{O_2}^{cl}$  (lower Knudsen effect). The design spacing increases from around  $R_v \approx 40$  nm at  $L_{Pt} = 0.3$  mg<sub>Pt</sub> cm<sup>-2</sup> (typical value found in CLs with the same loading (Wilson and Gottesfeld, 1992)) to  $R_v \sim 1000$  nm for exceedingly small Pt loadings,  $L_{Pt} \rightarrow 10^{-3}$  mg<sub>Pt</sub> cm<sup>-2</sup>. As a result,  $R_{O_2}^{cl}$  is reduced by an order of magnitude from  $\sim 10^{-2}$  s cm<sup>-1</sup> (similar to the resistance in water-filled nanopores,  $R_{O_2}^p$ ) down to  $\sim 10^{-3}$  s cm<sup>-1</sup> when the Pt loading is varied in the range  $L_{Pt} = 0.3-10^{-3}$  mg<sub>Pt</sub> cm<sup>-2</sup>.  $R_{O_2}^{cl}$  and  $R_{O_2}^p$  are around 2-3 orders of magnitude lower than the channel-CL and local oxygen resistances,  $R_{O_2,cl}^{ch}$  and  $R_{O_2,p}^{ion}$ , in conventional PEFCs with non-optimized CLs (Sánchez-Ramos et al., 2021). The volume fraction of electron-conductive material + Pt of the shell is small, growing from  $\varepsilon_{c+Pt}^{des} \sim 10^{-3}$  at  $L_{Pt} = 0.005$  mg<sub>Pt</sub> cm<sup>-2</sup> up to  $\varepsilon_{c+Pt}^{des} \approx 0.06$  at  $L_{Pt} \approx 0.3$  mg<sub>Pt</sub> cm<sup>-2</sup>. The increase of  $\varepsilon_{c+Pt}^{des}$  with  $L_{Pt}$  goes hand in hand with the increase of  $L^{des}$  since the thickness of the shell is fixed to  $L_p \ll L^{des}$ . The above results suggest that there is room to improve performance by optimizing CLs together with a reduction of oxygen transport resistance in passive porous layers of the MEA, flow field and stack flow distributor.

The optimal  $\tilde{R}_i$ , which arises from a trade-off between ionomer and void volume fractions ( $\varepsilon_i$  vs.  $\varepsilon$ ), is to be determined from numerical simulations. Figure 8A shows the power density,  $P$ , computed for the baseline case as a function of the ionomer volume fraction,  $\varepsilon_i = 0.05-0.8$ , and various Pt loadings,  $L_{Pt} = 0.005-0.3$  mg<sub>Pt</sub> cm<sup>-2</sup>.  $P$  slightly varies with  $\varepsilon_i$  except for exceedingly small ionomer volume fractions when the area available for proton transport is strongly reduced, i.e.,  $\sigma_p^{eff}$  is significantly decreased. A similar effect to that found in thin ionomer films. In a little more detail, it can be seen that the optimal ionomer volume fraction shifts to higher values as  $L_{Pt}$  is increased. This is explained by the larger secondary pore sizes reached with decreasing  $L_{Pt}$ , so the optimal design point is reached at a lower secondary porosity,  $\varepsilon$ . Nevertheless, the variations above  $\varepsilon_i \geq 0.2$  are almost negligible, so the design point was fixed to  $\tilde{R}_i = 0.3$  ( $\varepsilon_i \approx 0.3$ ) for subsequent analyses.

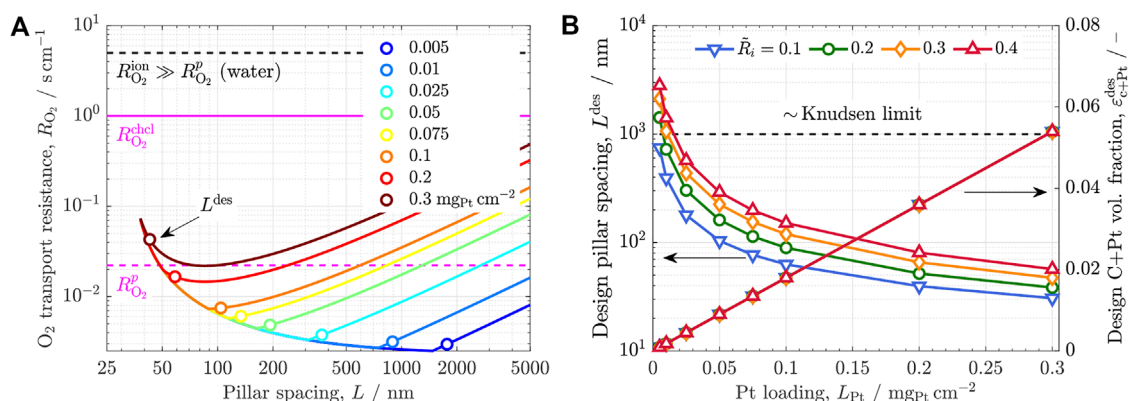


FIGURE 7

(A) Variation of the bulk O<sub>2</sub> transport resistance of the bi-functionalized bimodal cathode CL,  $R_{O_2}^{cl}$ , with the pillar spacing,  $L$ , corresponding to various Pt loadings,  $L_{Pt} = 0.005, 0.01, 0.025, 0.05, 0.075, 0.1, 0.2, 0.3$  mg<sub>Pt</sub> cm<sup>-2</sup>, and  $\bar{R}_i = 0.25$ . The figure also includes the O<sub>2</sub> transport resistance in optimized water-filled nanopores,  $R_{O_2}^p = L_p/D_{O_2,p}^{eff} \approx 0.02$  s cm<sup>-1</sup>, the channel-CL O<sub>2</sub> transport resistance of state-of-the-art PEMFCs (Owejan et al., 2013, 2014; Sun et al., 2020),  $R_{O_2}^{chd} \sim 1$  s cm<sup>-1</sup>, and the local O<sub>2</sub> transport resistance reported for non-optimized conventional CLs with ionomer thin films covering Pt nanoparticles at  $r_f \approx 1$  (Sánchez-Ramos et al., 2021),  $R_{O_2}^{ion} \sim 4.7$  s cm<sup>-1</sup>  $\gg R_{O_2}^p$  (water). The design spacing is selected for  $\delta_{cl} = \Pi \delta_{cl}^{min}$  ( $\Pi = 1.2$ ), close to the optimal point of minimum bulk and local transport resistances. (B) Variation of the design spacing,  $L^{des}$ , and the design volume fraction of electron-conductive material + Pt,  $\varepsilon_{C+Pt}$ , Pt loading,  $L_{Pt}$ , corresponding to  $\bar{R}_i = 0.1, 0.2, 0.3, 0.4$ . The Knudsen limit for which species diffusion is not significantly reduced is around 1000 nm.

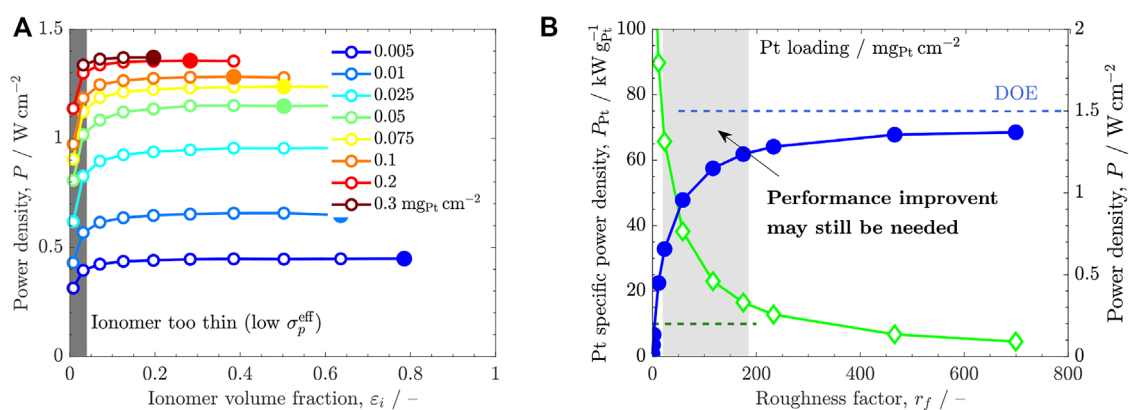
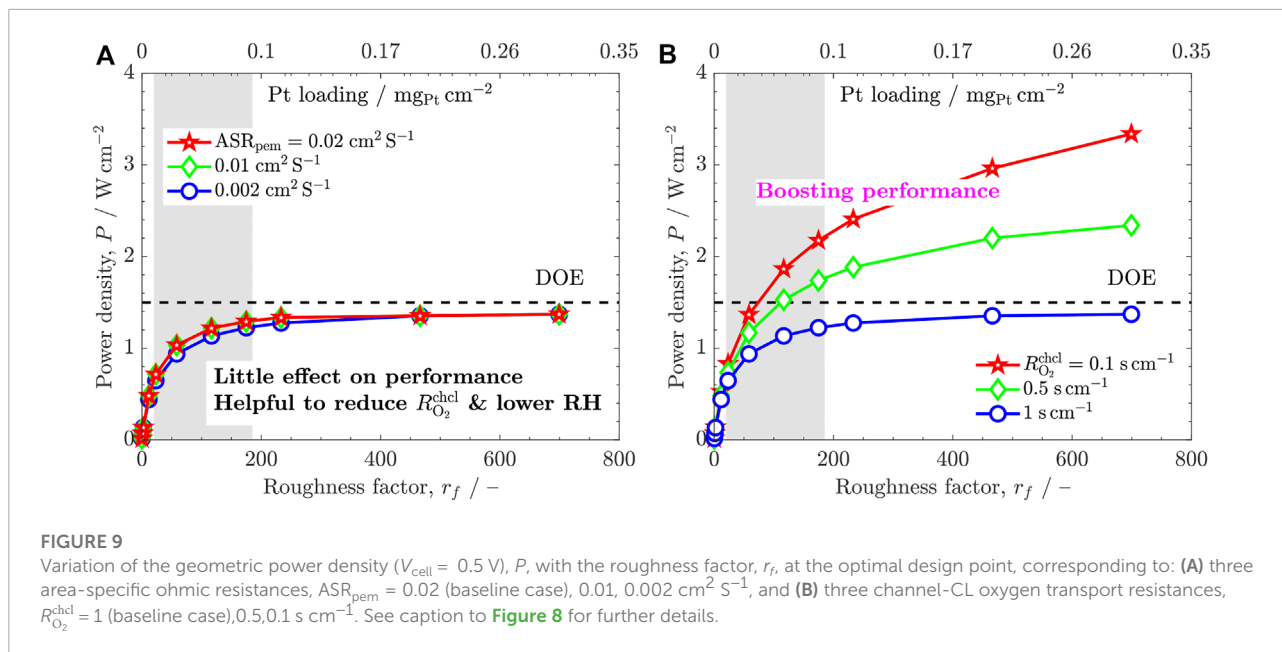


FIGURE 8

(A) Variation of the geometric power density,  $P$ , with the ionomer volume fraction,  $\varepsilon_i$ , at the design point of minimum transport resistance corresponding to several Pt loadings,  $L_{Pt} = 0.005 - 0.3$  mg<sub>Pt</sub> cm<sup>-2</sup>. The power density is reduced when  $\varepsilon_i$  is small because of the drop of  $\sigma_p^{eff}$  (bottleneck effect caused by too thin ionomer pillars). The computed optimal ionomer volume fractions are highlighted by big solid dots. (B) Variation of the Pt mass-specific power density and geometric power density ( $V_{cell} = 0.5$  V),  $P_{Pt}$  and  $P$ , respectively, with the roughness factor,  $r_f$ , at the optimal CL design point. The corresponding Pt loading is shown on the top axis,  $L_{Pt} = r_f \delta_{Pt} \rho_{Pt}$ ;  $\delta_{Pt} = 0.2$  nm. The DOE power density target at rated power (1 W cm<sup>-2</sup> @ 0.76 V,  $T = 80^\circ$ C) has been extrapolated to the examined voltage (1.5 W cm<sup>-2</sup> @ 0.5 V) (DOE, 2015).

Figure 8B shows the variation of the Pt-specific and geometric power densities,  $P_{Pt}$  and  $P$ , with the roughness factor,  $r_f$ , at the optimal design point ( $\bar{R}_i = 0.3$ ). The Pt loading corresponding to  $r_f$  in the optimized CL is indicated on the top axis (ECSA  $\approx 200$  m<sup>2</sup> g<sub>Pt</sub><sup>-1</sup>). The Pt-specific power density increases abruptly with decreasing  $L_{Pt}$  because of the steep  $P$ - $r_f$  relationship prevailing at low Pt loading. Although the limit  $p = 0$  at  $L_{Pt} = 0$  is inevitable (no reaction, no operation), the current density sharply increases when  $r_f > 0$  if there are no huge

transport resistances and/or the ECSA is too small. The increase of  $P$  with  $r_f$  flattens for high roughness factors ( $r_f \geq 100$ ) due to the effect of mass and ohmic resistances of the cathode CL and exterior components. Note that the limiting current density would be mainly controlled by  $R_{O_2}^{chd}$  if interior mass transport resistances in the CL are negligible and the roughness factor is extremely high ( $r_f \rightarrow \infty$ ). Maximizing the performance in the range  $L_{Pt} \approx 0.01-0.1$  mg<sub>Pt</sub> cm<sup>-2</sup> to meet the ultimate DOE targets may require an integral optimization of oxygen transport



resistances (see **Section 6.2** below). In terms of the cathode CL, increasing the fraction of water-based triple phase points provides a viable route to reach Pt-specific power densities between  $P_{\text{Pt}} \approx 10 - 40\text{ kW g}_{\text{Pt}}^{-1}$  and surpass the DOE target of  $10\text{ kW g}_{\text{Pt}}^{-1}$ , as recently demonstrated by The General Motors Company (Yarlagadda et al., 2018).

## 6.2 Effect of external transport resistances

The effect of the exterior ohmic and mass transport resistances,  $\text{ASR}_{\text{pem}}$  and  $R_{\text{O}_2}^{\text{chcl}}$ , on the geometrical power density at the optimal design point is examined in **Figures 9A,B**, respectively. Improvement of  $P$  at low  $L_{\text{Pt}}$  by a direct reduction of ohmic losses is not feasible, since thin PEMs currently used in PEMFCs (e.g., reinforced Nafion) with small thickness ( $\delta_{\text{pem}} \sim 10 - 30\text{ }\mu\text{m}$ ) and high ionic conductivity ( $\sigma_{\text{pem}} \approx 10 - 20\text{ S m}^{-1}$  at  $\text{RH} = 1$ ) have already been highly optimized and represent a rather small fraction of voltage losses,  $\Delta V_{\text{ohm}} \approx 0.02\text{ V}$  ( $I^{\text{avg}} \approx 2\text{ A cm}^{-2}$ )  $\ll E_r \approx 1.2\text{ V}$ . Moreover, thin PEMs can suffer from insufficient durability (e.g., ultra-thin GORE-SELECT PEMs (Kienitz et al., 2011)). As shown in **Figure 9B**, the power density is not significantly increased even when  $\text{ASR}_{\text{pem}}$  is decreased by an order of magnitude down to  $0.002\text{ cm}^2\text{ S}^{-1}$ , which is comparable to the resistance of an ultra-thin PEM  $1\text{ }\mu\text{m}$  thick without significant interfacial resistances. Nevertheless, a reduction of the PEM thickness can be useful to enhance water back diffusion to the anode and improve performance at low RH (Zhu et al., 2006; Steinbach et al., 2010). For instance, a thin reinforced PEM ( $\delta_{\text{pem}} \approx 10\text{ }\mu\text{m}$ ) was

incorporated in the Toyota Mirai in 2015, presumably to help alleviating cathode flooding at middle-to-high current density and making operation possible without external humidification (Yoshida and Kojima, 2015; Borup et al., 2018). By way of contrast, the impact of the channel-CL oxygen transport resistance is significantly larger, being crucial to reduce it to enhance performance at low  $L_{\text{Pt}}$ . A comparison of the external transport resistances against the layer-scale and nanoscale transport resistances in the CL leads to

$$\Gamma_{\text{O}_2,p}^{\text{chcl}} = \frac{R_{\text{O}_2}^{\text{chcl}}}{R_{\text{O}_2}^p} \sim \frac{10 - 10^2\text{ s m}^{-1}}{1 - 10^2\text{ s m}^{-1}} \sim 10^{-2} (r_f \sim 1) - 10^2 (r_f \sim 10^2) \quad (41a)$$

$$\Gamma_{\text{O}_2,cl}^{\text{chcl}} = \frac{R_{\text{O}_2}^{\text{chcl}}}{R_{\text{O}_2}^{\text{cl}}} \sim \frac{10 - 10^2\text{ s m}^{-1}}{10^{-1} - 1\text{ s m}^{-1}} \sim 10^2 - 10^3 \quad (41b)$$

$$\Gamma_{p,p}^{\text{pem}} = \frac{\text{ASR}_{\text{pem}}}{\text{ASR}_p} \sim \frac{10^{-7} - 10^{-6}\text{ m}^2\text{ S}^{-1}}{10^{-7} - 10^{-5}\text{ m}^2\text{ S}^{-1}} \sim 10^{-1} - 1 \quad (41c)$$

$$\Gamma_{p,cl}^{\text{pem}} = \frac{\text{ASR}_{\text{pem}}}{\text{ASR}_p^{\text{cl}}} \sim \frac{10^{-7} - 10^{-6}\text{ m}^2\text{ S}^{-1}}{10^{-7} - 10^{-6}\text{ m}^2\text{ S}^{-1}} \sim 1 \quad (41d)$$

From the above calculations, it turns out that the exterior and nanoscale oxygen transport resistances,  $R_{\text{O}_2}^{\text{chcl}}$  and  $R_{\text{O}_2}^p$ , are the most important ones. The bulk oxygen transport resistance of the CL,  $R_{\text{O}_2}^{\text{cl}}$ , can be more easily optimized to make its contribution negligible provided that there are no flooding-related issues (see **Figure 7**) (Conde et al., 2019; Talukdar et al., 2019). The contribution of  $R_{\text{O}_2}^{\text{chcl}}$  dominates the performance of the optimized CL when  $r_f \geq 10$  ( $R_{\text{O}_2}^p$  cannot be neglected at



$r_f \sim 1-10$ ). The effect of ohmic losses in the CL is comparable to that of  $ASR_{pem}$  and can be neglected to optimize the performance at low  $L_{Pt}$  under normal conditions, as commented before.

Power densities above  $1.5 \text{ W cm}^{-2}$  are predicted with air feed at low Pt loading with a ten-fold reduction of the external oxygen resistance from  $R_{O_2}^{chl} \approx 1 \text{ s cm}^{-1}$  to  $R_{O_2}^{chl} \approx 0.1 \text{ s cm}^{-1}$ . Decreasing  $R_{O_2}^{chl}$  by one order of magnitude may require a highly optimized design of the cathode MEA/flow field/stack architecture. An example is the highly engineered 3D porous cathode flow field and thin GDLs ( $\delta_{gdl} \approx 150 \mu\text{m}$ ) incorporated in the Toyota Mirai to boost the performance of previously developed designs up to  $3-4 \text{ A cm}^{-2}$  ( $L_{Pt} \approx 0.3 \text{ mg}_{Pt} \text{ cm}^{-2}$ ) (Yoshida and Kojima, 2015). Water management at the cathode was also probably helped by the thin PEM and reduced humidification. The optimized component-architecture-operation design of the Toyota Mirai provides a good basis for subsequent reductions of the Pt loading via CL optimization. However, the fabrication of flow fields and stacks with complex 3D geometries using conventional methods is not desirable for large production. Work is still needed to develop alternative strategies for decreasing  $R_{O_2}^{chl}$  at high current density using standard procedures, e.g., porous flow fields, flow fields with narrower channels and/or GDL-MPLs with tailored thickness and wettability (Jiao et al., 2021), or advanced manufacturing techniques, such as multiscale 3D printing of metal powders (e.g., Ti, stainless steel and Ni (Yi et al., 2012; Choi et al., 2014; Ercelik et al., 2022)) and alternative raw material powders (3D printing can also help in reducing electrical contact resistances and inhomogeneous assembly compression (García-Salaberri et al., 2011, 2018, 2019; García-Salaberri P. A. et al., 2017; Hack et al., 2020)). In particular, decreasing the thickness of GDLs and flow fields by integrating them into a single component can enable the production of more compact stacks, reducing weight and increasing volumetric current density, as recently demonstrated by Korean researchers (Park et al., 2019). Another option to improve cathode performance would be to use a more efficient compressor to increase the cathode pressure, while avoiding a reduction of the system efficiency (Sery and Leduc, 2022).

### 6.3 Effect of catalyst activity (exchange current density)

The last option to improve performance within DOE targets is catalyst modification by: 1) increasing the mass activity with the same amount of precious metals, and 2) maintaining the mass activity with a reduced amount of precious metals (or a combination of both). According to Tafel equation, for a given roughness factor and overpotential, a catalyst with a higher exchange current density can potentially increase the current

density in the same proportion (if transport losses are small)

$$I^{avg} = r_f I_p^{avg}, \quad \frac{I_{p,2}^{avg}}{I_{p,1}^{avg}} = \frac{i_{o,c,2}}{i_{o,c,1}} C_{O_2}, \quad \eta_c \approx \text{cte.} \quad (42)$$

Figure 10 shows the variation of  $P$  with  $r_f$  for three different exchange current densities,  $i_{o,c} = 0.5, 1, 5 \text{ A m}_{Pt}^{-2}$ , corresponding to high and low external oxygen transport resistances, 1)  $R_{O_2}^{chl} = 1 \text{ s cm}^{-1}$  and 2)  $R_{O_2}^{chl} = 0.01 \text{ s cm}^{-1}$ . According to Eq. 42, increasing  $i_{o,c}$  is useful to boost performance at middle-to-high current density when oxygen transport to the cathode CL is facilitated. In this case, the combination of a high average oxygen concentration and a high exchange current density can significantly raise the power density to around  $2 \text{ W cm}^{-2}$  at low  $L_{Pt}$ . The performance improvement in practice will largely depend on the increase of  $i_{o,c}$  that can be achieved and the ability to keep  $R_{O_2}^{chl}$  small at high water production rates (special attention is to be devoted to efficient water removal in vapor form with increasing heat generation). In contrast, when oxygen transport to the CL is hindered, the beneficial effect of increasing  $i_{o,c}$  is strongly reduced since operation at high performance is no longer possible due to oxygen starvation. As shown in Figure 11A, the limiting current density remains the same regardless of the exchange current density for  $R_{O_2}^{chl} = 1 \text{ s cm}^{-1}$ , while no limiting current density is present in the voltage range examined for  $R_{O_2}^{chl} = 0.01 \text{ s cm}^{-1}$ . The average oxygen concentration in the cathode CL,  $C_{O_2,cl}^{avg}$ , closely follows the linear relationship given by  $R_{O_2}^{chl}$  due to the reduced effect of other transport resistances in the optimized CL design (see Figure 11B).

As a final remark, it is relevant to examine the limit to which  $L_{Pt}$  might be reduced to ensure a certain minimum performance. The frontier is largely controlled by  $r_f$ . As shown in Figure 10B, the power density with a highly optimized PEMFC (i.e., CL based on water-filled triple phase points,  $\times 0.1 R_{O_2}^{chl}$ ,  $\times 10 i_{o,c}$  with respect to the state of the art and negligible losses at the anode) dramatically drops when  $r_f \lesssim 10$ , being impossible to meet DOE targets when  $r_f \lesssim 1$  (similar electrochemical and geometrical areas). The positive effect of increasing  $i_{o,c}$  and  $C_{O_2,cl}^{avg}$  is dramatically reduced when  $r_f \lesssim 1$  because  $I_p^{avg}$  becomes too small even if all transport resistances are minimized. Considering the Tafel equation again, the maximum possible current density at a given overpotential is equal to

$$I^{avg} \sim I_p^{avg} \sim i_{o,c} \left( \frac{C_{O_2,p}^{in}}{C_{O_2}^{ref}} \right)^{\gamma} \exp \left[ -\frac{\alpha_c F}{R^o T} \eta_c \right] \quad (43)$$

where  $C_{O_2,p}^{in} \sim k_{H_2O_2,w} C_{O_2,chl}^{in}$  is the oxygen concentration at the entrance of nanopores. For  $\eta_c \approx -(0.5-0.4) \text{ V}$  ( $V_{cell} \approx 0.5 \text{ V}$ ), we yield  $I^{avg} \sim I_p^{avg} \sim 10^{-2} \text{ A cm}^{-2}$  at  $r_f \sim 1$ . Interestingly, the region where operation at high performance is hardly complicated is adjacent to the ultimate DOE target corresponding to

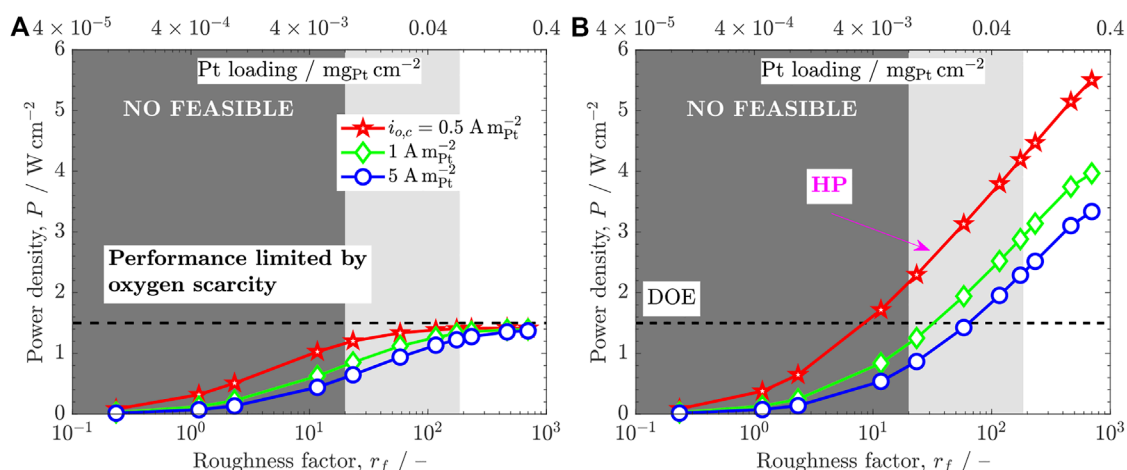


FIGURE 10

Variation of the geometric power density ( $V_{\text{cell}} = 0.5 \text{ V}$ ),  $P$ , with the roughness factor,  $r_f$ , at the optimized design point for three exchange current densities,  $i_{o,c} = 0.5, 1, 5 \text{ A m}_{\text{Pt}}^{-2}$ , corresponding to: (A) state-of-the-art channel-CL oxygen transport resistance,  $R_{\text{O}_2}^{\text{chl}} = 1 \text{ s cm}^{-1}$ , and (B) optimized channel-CL oxygen transport resistance,  $R_{\text{O}_2}^{\text{chl}} = 0.1 \text{ s cm}^{-1}$ . See caption to Figure 8 for further details.

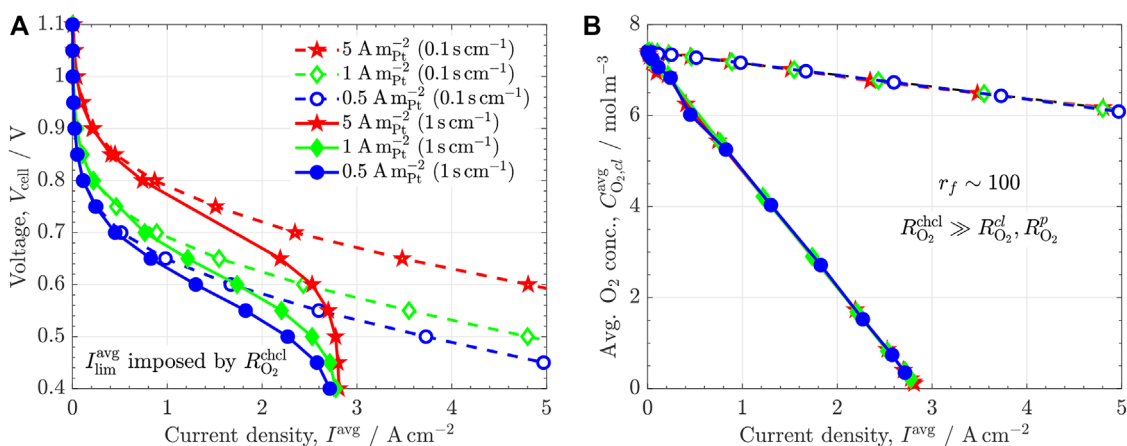


FIGURE 11

(A) Polarization curve,  $V_{\text{cell}} - I^{\text{avg}}$ , and (B) variation of the average oxygen concentration in the CL,  $C_{\text{O}_2,\text{ct}}^{\text{avg}}$ , with the average current density,  $I^{\text{avg}}$ , at  $r_f \sim 100$  ( $L_{\text{Pt}} = 0.05 \text{ mg}_{\text{Pt}} \text{ cm}^{-2}$ ). The results for three exchange current densities,  $i_{o,c} = 0.5, 1, 5 \text{ A m}_{\text{Pt}}^{-2}$ , corresponding to both high and low channel-CL oxygen resistances,  $R_{\text{O}_2}^{\text{chl}} = 1 \text{ s cm}^{-1}$  and  $R_{\text{O}_2}^{\text{chl}} = 0.1 \text{ s cm}^{-1}$ , are included.

the idealized high ECSA cathode CL examined here (weak  $L_{\text{Pt}} - r_f$  relationship). This result highlights the importance of maximizing the ECSA and facilitating oxygen transport toward the cathode CL, while keeping  $r_f \geq 10$  using highly active Pt-alloys with a reduced Pt content if needed.

## 7 Conclusion

The performance and durability of proton exchange fuel cells (PEFCs) is largely linked to an optimal design of the

cathode catalyst layer (CL), especially if a reduction of the Pt loading ( $L_{\text{Pt}} \sim 10^{-2} \text{ mg}_{\text{Pt}} \text{ cm}^{-2}$ ) is desired to meet industrial requirements in terms of design and cost (e.g., ultimate targets set by the U.S. Department of Energy to make PEFC technology competitive). Based on the analysis conducted in this work, good practices to enhance the performance and enlarge the durability of the cathode CL at low Pt loading are as follows:

- 1) To increase the electrochemical surface area, ECSA, as much as possible to decrease the Pt loading needed to achieve a specified roughness factor,  $r_f$ . Reaching high performance (say, beyond  $P \approx 1.5 \text{ W cm}^{-2}$ ) at low Pt loading

with  $r_f \leq 10$  can be difficult due to the sluggishness of the oxygen reduction reaction (ORR). An increase of the catalyst active area up to  $\text{ECSA} \sim 100 \text{ m}^2 \text{ g}_{\text{Pt}}^{-1}$  (e.g., through a combination of small Pt nanoparticles or atomic skins and highly accessible nanoporous structures) can allow a reduction of the Pt loading down to  $0.05 \text{ mg}_{\text{Pt}} \text{ cm}^{-2}$  ( $r_f \sim 100$ ) and  $0.005 \text{ mg}_{\text{Pt}} \text{ cm}^{-2}$  ( $r_f \sim 10$ ). The decrease of  $r_f$  at low Pt loading can additionally be alleviated using active Pt-alloys (e.g., PtCo) if a further increase in ECSA is not feasible.

- 2) To increase the percentage of triple phase points based on water-filled nanopores with no entry mass transport losses caused by (thin) ionomer films. Modification of nanoporous supports with short transport lengths ( $\sim 10 \text{ nm}$ ) can be a viable route to increase the Pt-specific power density above  $P_{\text{Pt}} \sim 10 \text{ kW g}_{\text{Pt}}^{-1}$ . Optimized CLs with bi-functionalized microstructures (i.e., with a (precise) separation of mass and proton transport domains) and bimodal pore size distributions (i.e., with tailored primary nanopores to promote water adsorption and capillary condensation, and secondary pores to facilitate water removal) is crucial. If a high degree of bi-functionalization of the CL is not possible, the development of ionomers with tailored mass and ionic transport resistances can be useful. Novel ionomers can reduce entry mass transport resistances at the nanoscale, while allowing good proton conduction at the layer scale.
- 3) To reduce the oxygen transport resistance from the channel to the CL (i.e., from the stack inlet(s) to the CL),  $R_{\text{O}_2}^{\text{chcl}}$ , especially at high current density. Optimization of the oxygen transport resistance in other components, such as the stack flow distributor, flow field, gas diffusion layer and microporous layer, can be necessary to reach power densities above  $P = 1.5 \text{ W cm}^{-2}$  at low Pt loading. Although solving the problem of the local oxygen transport resistance of ionomer in conventional cathode CLs is mandatory ( $R_{\text{O}_2,p}^{\text{ion}} \approx 0.4 - 4 \text{ s cm}^{-1}$  at  $r_f \approx 10-1$ ), the performance can be limited by exterior oxygen transport resistances once  $R_{\text{O}_2,p}^{\text{ion}}$  is significantly decreased or even removed using bi-functionalized bimodal microstructures ( $R_{\text{O}_2,p} \approx 0.02 \text{ s cm}^{-1}$ ). A ten-fold decrease of the exterior oxygen transport resistance from  $R_{\text{O}_2}^{\text{chcl}} \approx 1 \text{ s cm}^{-1}$  (conventional value) down to  $R_{\text{O}_2}^{\text{chcl}} \approx 0.1 \text{ s cm}^{-1}$  (highly optimized cathode flow distributor) can allow power densities around  $P \approx 2 \text{ W cm}^{-2}$  at  $L_{\text{Pt}} \approx 0.05 \text{ mg}_{\text{Pt}} \text{ cm}^{-2}$ . Ohmic losses play a secondary role to enhance performance at low Pt loading, but thin membranes can be used to promote back diffusion and improve water management.
- 4) Increasing the catalyst mass activity (exchange current density,  $i_{o,c}$ ) can allow an improvement of the power density if other transport losses do not limit the cell performance. Increasing  $i_{o,c}$  ( $\times 10$ ) in combination with a reduction of  $R_{\text{O}_2}^{\text{chcl}}$  ( $\times 0.1$ ) and CL optimization can raise the power density

up to  $P \approx 2-3 \text{ W cm}^{-2}$  at low Pt loading, even though this will require an optimized water management strategy to keep  $R_{\text{O}_2}^{\text{chcl}}$  small. Increasing  $i_{o,c}$  without reducing  $R_{\text{O}_2}^{\text{chcl}}$  can significantly limit the performance gain.

- 5) Durability during dynamic operation can be increased if corrosion of the carbon support is avoided at the cathode. Polymer and metallic (e.g.,  $\text{T}_1\text{O}_2$ ) supports show a longer durability than carbon-based supports (e.g., carbon black, graphite or carbon nanotubes). However, an economic analysis is needed to quantify if a change of the support to more expensive materials (e.g.,  $\text{T}_1\text{O}_2$ ) is cost-effective.

Although commercialization of PEMFCs is underway for some applications, such as heavy-duty vehicles, trains, electric bicycles, etc., several aspects warrant future work to be addressed by a combination of experimental and numerical work. Research is expected to continue toward increasing performance and durability at low Pt loading, mainly for two reasons: 1) to examine the technology limits that could provide a more affordable and extended use in general purpose applications, and 2) to leverage the development of cheap, durable, high-performance PEMFCs for light-duty vehicles that can make the technology more competitive in the automotive sector. As exemplified in this work, research topics to be analyzed in more detail include: 1) reduction of Pt loading *via* optimization of the multiscale microstructure of CLs, 2) water management with a focus on CL design and interaction with other layers, 3) reduction of oxygen transport resistance in MEAs and stacks, 4) increasing durability of carbon-based supports through a reduction of carbon corrosion, and 5) simplification of balance of plant. An effort is to be made toward integrated, multidisciplinary work, since most of these topics are coupled with each other. This probably explains why most significant recent developments in PEMFC technology were accomplished by companies, while research in the field seems to be a scattered combination of chemical, electrical, electrochemical and mechanical engineering, among other disciplines. Modeling is an essential transversal tool for understanding and optimization.

## Data availability statement

The raw data supporting the conclusion of this article will be made available by the authors, without undue reservation.

## Author contributions

GS contributed to the conception and design of the study, the simulation campaign, and the writing of the first draft of the manuscript. All authors contributed to manuscript revision, read, and approved the submitted version.

## Funding

This work was supported by projects PID2019-106740RB-I00 and EIN 2020-112247 of the Spanish Research Council.

## Acknowledgments

GS acknowledges fruitful discussion with Dr. Adam Z. Weber at Lawrence Berkeley National Lab under the framework of the project “Multiphysics, Multiphase and Multiscale Modeling of Porous Media with Application to Energy Conversion and Storage Electrochemical Devices” granted by the Spanish Research Council.

## References

- Antolini, E., and Gonzalez, E. (2009). Ceramic materials as supports for low-temperature fuel cell catalysts. *Solid State Ionics* 180, 746–763. doi:10.1016/j.ssi.2009.03.007
- Atanassov, P., Di Noto, V., and McPhail, S. (2021). From hydrogen manifesto, through green deal and just transition, to clean energy act. *Electrochem. Soc. Interface* 30, 57–60. doi:10.1149/2.f14214if
- Attari Moghaddam, A., Prat, M., Tsotsas, E., and Kharaghani, A. (2017). Evaporation in capillary porous media at the perfect piston-like invasion limit: Evidence of nonlocal equilibrium effects. *Water Resour. Res.* 53, 10433–10449. doi:10.1002/2017wr021162
- Avcioglu, G. S., Ficicilar, B., and Eroglu, I. (2016). Effect of ptfe nanoparticles in catalyst layer with high pt loading on pem fuel cell performance. *Int. J. Hydrogen Energy* 41, 10010–10020. doi:10.1016/j.ijhydene.2016.03.048
- Azarfa, A., Ismail, M. S., Rezakazemi, M., and Pourkashanian, M. (2019). Comparative study of conventional and unconventional designs of cathode flow fields in pem fuel cell. *Renew. Sustain. Energy Rev.* 116, 109420. doi:10.1016/j.rser.2019.109420
- Babu, S. K., Mukundan, R., Wang, C., Langlois, D., Cullen, D. A., Papadias, D., et al. (2021). Effect of catalyst and catalyst layer composition on catalyst support durability. *J. Electrochem. Soc.* 168, 044502. doi:10.1149/1945-7111/abf21f
- Blunier, B., Gao, F., and Miraoui, A. (2013). *Proton exchange membrane fuel cells modeling*. John Wiley & Sons.
- Borup, R. L., Kusoglu, A., Neyerlin, K. C., Mukundan, R., Ahluwalia, R. K., Cullen, D. A., et al. (2020). Recent developments in catalyst-related pem fuel cell durability. *Curr. Opin. Electrochem.* 21, 192–200. doi:10.1016/j.coelec.2020.02.007
- Borup, R. L., More, K. L., and Myers, D. J. (2018). Fc-pad: Fuel cell performance and durability consortium update to uscar analysis of toyota mirai components provided by uscar
- Borup, R., and Weber, A. (2019). *Fc135: Fc-pad: Fuel cell performance and durability consortium*. Washington DC: Annual Merit Review Proceedings.
- Chen, D., Kongkanand, A., and Jorne, J. (2019). Proton conduction and oxygen diffusion in ultra-thin nafion films in pem fuel cell: How thin? *J. Electrochem. Soc.* 166, F24–F33. doi:10.1149/2.0101902jes
- Chen, K., Deng, S., Lu, Y., Gong, M., Hu, Y., Zhao, T., et al. (2021). Molybdenum-doped titanium dioxide supported low-pt electrocatalyst for highly efficient and stable hydrogen evolution reaction. *Chin. Chem. Lett.* 32, 765–769. doi:10.1016/j.ccllet.2020.05.030
- Chen, M., Zhao, C., Sun, F., Fan, J., Li, H., and Wang, H. (2020). Research progress of catalyst layer and interlayer interface structures in membrane electrode assembly (mea) for proton exchange membrane fuel cell (pemfc) system. *ETransportation* 5, 100075. doi:10.1016/j.etrans.2020.100075
- Chen, Z., Deng, W., Wang, X., and Yan, Y. (2007). Durability and activity study of single-walled, double-walled and multi-walled carbon nanotubes supported pt catalyst for pemfcs. *ECS Trans.* 11, 1289–1299. doi:10.1149/1.2781042
- Cheng, X., Shen, S., Wei, G., Wang, C., Luo, L., and Zhang, J. (2022). Perspectives on challenges and achievements in local oxygen transport of low pt proton exchange membrane fuel cells. *Adv. Mat. Technol.* 7, 2200228. doi:10.1002/admt.202200228
- Chi, B., Hou, S., Liu, G., Deng, Y., Zeng, J., Song, H., et al. (2018). Tuning hydrophobic-hydrophilic balance of cathode catalyst layer to improve cell performance of proton exchange membrane fuel cell (pemfc) by mixing polytetrafluoroethylene (ptfe). *Electrochimica Acta* 277, 110–115. doi:10.1016/j.electacta.2018.04.213
- Choi, H., Kim, O.-H., Kim, M., Choe, H., Cho, Y.-H., and Sung, Y.-E. (2014). Next-generation polymer-electrolyte-membrane fuel cells using titanium foam as gas diffusion layer. *ACS Appl. Mat. Interfaces* 6, 7665–7671. doi:10.1021/am500962h
- Cochet, M., Forner-Cuenca, A., Manzi-Orezzoli, V., Siegwart, M., Scheuble, D., and Boillat, P. (2020). Enabling high power density fuel cells by evaporative cooling with advanced porous media. *J. Electrochem. Soc.* 167, 084518. doi:10.1149/1945-7111/ab8e82
- Conde, J. J., Folgado, M. A., Ferreira-Aparicio, P., Chaparro, A. M., Chowdhury, A., Kusoglu, A., et al. (2019). Mass-transport properties of electrosprayed pt/c catalyst layers for polymer-electrolyte fuel cells. *J. Power Sources* 427, 250–259. doi:10.1016/j.jpowsour.2019.04.079
- Cui, L., Zhang, J., Wang, H., Lu, S., and Xiang, Y. (2021). The effects of different dimensional carbon additives on performance of pemfc with low-pt loading cathode catalytic layers. *Int. J. Hydrogen Energy* 46, 15887–15895. doi:10.1016/j.ijhydene.2021.02.032
- Debe, M. K., Atanasoski, R. T., and Steinbach, A. J. (2011). Nanostructured thin film electrocatalysts-current status and future potential. *ECS Trans.* 41, 937–954. doi:10.1149/1.3635628
- Debe, M. K. (2011). Effect of electrode surface area distribution on high current density performance of pem fuel cells. *J. Electrochem. Soc.* 159, B53–B66. doi:10.1149/2.032201jes
- Debe, M. K. (2012). Nanostructured thin film electrocatalysts for pem fuel cells-a tutorial on the fundamental characteristics and practical properties of nsff catalysts. *ECS Trans.* 45, 47–68. doi:10.1149/1.3701968
- Debe, M. K., Schmoekel, A. K., Vernstrom, G. D., and Atanasoski, R. (2006). High voltage stability of nanostructured thin film catalysts for pem fuel cells. *J. Power Sources* 161, 1002–1011. doi:10.1016/j.jpowsour.2006.05.033
- Deng, X., Huang, C., Pei, X., Hu, B., and Zhou, W. (2021). Recent progresses and remaining issues on the ultrathin catalyst layer design strategy for high-performance proton exchange membrane fuel cell with further reduced pt loadings: A review. *Int. J. Hydrogen Energy* 47, 1529–1542. doi:10.1016/j.ijhydene.2021.10.141

## Conflict of interest

The authors declare that the research was conducted in the absence of any commercial or financial relationships that could be construed as a potential conflict of interest.

## Publisher's note

All claims expressed in this article are solely those of the authors and do not necessarily represent those of their affiliated organizations, or those of the publisher, the editors and the reviewers. Any product that may be evaluated in this article, or claim that may be made by its manufacturer, is not guaranteed or endorsed by the publisher.



- DOE (2015). Hydrogen and fuel cell technologies office multi-year research, development, and demonstration plan. Available at: <https://www.energy.gov/eere/fuelcells/articles/hydrogen-and-fuel-cell-technologies-office-multi-year-research-development>.
- Ercelik, M., Ismail, M. S., Ingham, D. B., Hughes, K. J., Ma, L., and Pourkashanian, M. (2022). Efficient x-ray ct-based numerical computations of structural and mass transport properties of nickel foam-based gdl for pefcs. *Energy* 262, 125531. doi:10.1016/j.energy.2022.125531
- Esfahani, R. A. M., and Easton, E. B. (2020). Exceptionally durable pt/toms catalysts for fuel cells. *Appl. Catal. B Environ.* 268, 118743. doi:10.1016/j.apcatb.2020.118743
- Esfahani, R. A. M., Ebraldiz, I. I., Specchia, S., and Easton, E. B. (2018). A fuel cell catalyst support based on doped titanium suboxides with enhanced conductivity, durability and fuel cell performance. *J. Mat. Chem. A Mat.* 6, 14805–14815. doi:10.1039/c8ta02470g
- Folgado, M., Conde, J., Ferreira-Aparicio, P., and Chaparro, A. (2018). Single cell study of water transport in pemfcs with electrosprayed catalyst layers. *Fuel Cells* 18, 602–612. doi:10.1002/fuce.201700217
- Fumagalli, M., Lyonard, S., Prajapati, G., Berrod, Q., Porcar, L., Guillermo, A., et al. (2015). Fast water diffusion and long-term polymer reorganization during nafion membrane hydration evidenced by time-resolved small-angle neutron scattering. *J. Phys. Chem. B* 119, 7068–7076. doi:10.1021/acs.jpcc.5b01220
- García-Salaberri, P. A. (2022). “General aspects in the modeling of fuel cells: From conventional fuel cells to nano fuel cells,” in *Nanotechnology in fuel cells* (Elsevier), 77
- García-Salaberri, P. A., Gostick, J. T., Hwang, G., Weber, A. Z., and Vera, M. (2015a). Effective diffusivity in partially-saturated carbon-fiber gas diffusion layers: Effect of local saturation and application to macroscopic continuum models. *J. Power Sources* 296, 440–453. doi:10.1016/j.jpowsour.2015.07.034
- García-Salaberri, P. A., Gostick, J. T., Zenyuk, I. V., Hwang, G., Vera, M., and Weber, A. Z. (2017b). On the limitations of volume-averaged descriptions of gas diffusion layers in the modeling of polymer electrolyte fuel cells. *ECS Trans.* 80, 133–143. doi:10.1149/08008.0133ecst
- García-Salaberri, P. A., Hwang, G., Vera, M., Weber, A. Z., and Gostick, J. T. (2015b). Effective diffusivity in partially-saturated carbon-fiber gas diffusion layers: Effect of through-plane saturation distribution. *Int. J. Heat Mass Transf.* 86, 319–333. doi:10.1016/j.ijheatmasstransfer.2015.02.073
- García-Salaberri, P. A., Vera, M., and Zaera, R. (2011). Nonlinear orthotropic model of the inhomogeneous assembly compression of pem fuel cell gas diffusion layers. *Int. J. Hydrogen Energy* 36, 11856–11870. doi:10.1016/j.ijhydene.2011.05.152
- García-Salaberri, P. A., Zenyuk, I. V., Hwang, G., Vera, M., Weber, A. Z., and Gostick, J. T. (2019). Implications of inherent inhomogeneities in thin carbon fiber-based gas diffusion layers: A comparative modeling study. *Electrochimica Acta* 295, 861–874. doi:10.1016/j.electacta.2018.09.089
- García-Salaberri, P. A., Zenyuk, I. V., Shum, A. D., Hwang, G., Vera, M., Weber, A. Z., et al. (2018). Analysis of representative elementary volume and through-plane regional characteristics of carbon-fiber papers: Diffusivity, permeability and electrical/thermal conductivity. *Int. J. Heat Mass Transf.* 127, 687–703. doi:10.1016/j.ijheatmasstransfer.2018.07.030
- García-Salaberri, P. (2021). Modeling diffusion and convection in thin porous transport layers using a composite continuum-network model: Application to gas diffusion layers in polymer electrolyte fuel cells. *Int. J. Heat Mass Transf.* 167, 120824. doi:10.1016/j.ijheatmasstransfer.2020.120824
- García-Salaberri, P., Sánchez, D., Boillat, P., Vera, M., and Friedrich, K. A. (2017a). Hydration and dehydration cycles in polymer electrolyte fuel cells operated with wet anode and dry cathode feed: A neutron imaging and modeling study. *J. Power Sources* 359, 634–655. doi:10.1016/j.jpowsour.2017.03.155
- Garsany, Y., Atkinson, R. W.III, Gould, B. D., and Swider-Lyons, K. E. (2018). High power, low-pt membrane electrode assemblies for proton exchange membrane fuel cells. *J. Power Sources* 408, 38–45. doi:10.1016/j.jpowsour.2018.10.073
- Gebel, G., Lyonard, S., Mendil-Jakani, H., and Morin, A. (2011). The kinetics of water sorption in nafion membranes: A small-angle neutron scattering study. *J. Phys. Condens. Matter* 23, 234107. doi:10.1088/0953-8984/23/23/234107
- Gomaa, M. M., Sánchez-Ramos, A., Ureña, N., Pérez-Prior, M. T., Levenfeld, B., García-Salaberri, P. A., et al. (2022). Characterization and modeling of free volume and ionic conduction in multiblock copolymer proton exchange membranes. *Polymers* 14, 1688. doi:10.3390/polym14091688
- Goshtasbi, A., García-Salaberri, P., Chen, J., Talukdar, K., Sanchez, D. G., and Ersal, T. (2019). Through-the-membrane transient phenomena in pem fuel cells: A modeling study. *J. Electrochem. Soc.* 166, F3154–F3179. doi:10.1149/2.0181907jes
- Gostick, J. T., and Weber, A. Z. (2015). Resistor-network modeling of ionic conduction in polymer electrolytes. *Electrochimica Acta* 179, 137–145. doi:10.1016/j.electacta.2015.03.126
- Greszler, T. A., Caulk, D., and Sinha, P. (2012). The impact of platinum loading on oxygen transport resistance. *J. Electrochem. Soc.* 159, F831–F840. doi:10.1149/2.061212jes
- Hack, J., García-Salaberri, P. A., Kok, M. D., Jervis, R., Shearing, P. R., Brandon, N., et al. (2020). X-Ray micro-computed tomography of polymer electrolyte fuel cells: What is the representative elementary area? *J. Electrochem. Soc.* 167, 013545. doi:10.1149/1945-7111/ab6983
- Han, P., and Bartels, D. M. (1996). Temperature dependence of oxygen diffusion in H<sub>2</sub>O and D<sub>2</sub>O. *J. Phys. Chem.* 100, 5597–5602. doi:10.1021/jp952903y
- Huang, Z., Chen, B., Mo, X., Yang, X., Yu, L., Hu, X., et al. (2021). Fast water evaporation from nanopores. *Adv. Mat. Interfaces* 8, 2100660. doi:10.1002/admi.202100660
- Jiao, K., and Li, X. (2011). Water transport in polymer electrolyte membrane fuel cells. *Prog. Energy Combust. Sci.* 37, 221–291. doi:10.1016/j.pecs.2010.06.002
- Jiao, K., Xuan, J., Du, Q., Bao, Z., Xie, B., Wang, B., et al. (2021). Designing the next generation of proton-exchange membrane fuel cells. *Nature* 595, 361–369. doi:10.1038/s41586-021-03482-7
- Jomori, S., Nonoyama, N., and Yoshida, T. (2012). Analysis and modeling of pemfc degradation: Effect on oxygen transport. *J. Power Sources* 215, 18–27. doi:10.1016/j.jpowsour.2012.04.069
- Kienitz, B., Kolde, J., Priestler, S., Baczkowski, C., and Crum, M. (2011). Ultra-thin reinforced ionomer membranes to meet next generation fuel cell targets. *ECS Trans.* 41, 1521–1530. doi:10.1149/1.3635683
- Kim, S., and Mench, M. (2009). Investigation of temperature-driven water transport in polymer electrolyte fuel cell: Phase-change-induced flow. *J. Electrochem. Soc.* 156, B353. doi:10.1149/1.3046136
- Kobayashi, A., Fujii, T., Harada, C., Yasumoto, E., Takeda, K., Kakinuma, K., et al. (2021). Effect of pt and ionomer distribution on polymer electrolyte fuel cell performance and durability. *ACS Appl. Energy Mat.* 4, 2307–2317. doi:10.1021/acsaem.0c02841
- Kongkanand, A., and Mathias, M. F. (2016). The priority and challenge of high-power performance of low-platinum proton-exchange membrane fuel cells. *J. Phys. Chem. Lett.* 7, 1127–1137. doi:10.1021/acs.jpclett.6b00216
- Kulikovsky, A. (2010). The regimes of catalyst layer operation in a fuel cell. *Electrochimica Acta* 55, 6391–6401. doi:10.1016/j.electacta.2010.06.053
- Kusoglu, A., Kwong, A., Clark, K. T., Gunterman, H. P., and Weber, A. Z. (2012). Water uptake of fuel-cell catalyst layers. *J. Electrochem. Soc.* 159, F530–F535. doi:10.1149/2.031209jes
- Kusoglu, A., and Weber, A. Z. (2017). New insights into perfluorinated sulfonic acid ionomers. *Chem. Rev.* 117, 987–1104. doi:10.1021/acs.chemrev.6b00159
- Li, Y., Chen, H., Xiao, S., Alibakhshi, M. A., Lo, C.-W., Lu, M.-C., et al. (2019). Ultrafast diameter-dependent water evaporation from nanopores. *ACS Nano* 13, 3363–3372. doi:10.1021/acsnano.8b09258
- Lin, R., Wang, H., and Zhu, Y. (2021). Optimizing the structural design of cathode catalyst layer for pem fuel cells for improving mass-specific power density. *Energy* 221, 119909. doi:10.1016/j.energy.2021.119909
- Liu, C. P., Saha, P., Huang, Y., Shimpalee, S., Satjaritanun, P., and Zenyuk, I. V. (2021). Measurement of contact angles at carbon fiber–water–air triple-phase boundaries inside gas diffusion layers using x-ray computed tomography. *ACS Appl. Mat. Interfaces* 13, 20002–20013. doi:10.1021/acsmi.1c00849
- Liu, J., García-Salaberri, P. A., and Zenyuk, I. V. (2019a). Bridging scales to model reactive diffusive transport in porous media. *J. Electrochem. Soc.* 167, 013524. doi:10.1149/2.0242001jes
- Liu, J., García-Salaberri, P. A., and Zenyuk, I. V. (2019b). The impact of reaction on the effective properties of multiscale catalytic porous media: A case of polymer electrolyte fuel cells. *Transp. Porous Media* 128, 363–384. doi:10.1007/s11242-019-01252-8
- Liu, J., Gazzarri, J., and Eikerling, M. (2013). Model-based *ex situ* diagnostics of water fluxes in catalyst layers of polymer electrolyte fuel cells. *Fuel Cells* 13, 134–142. doi:10.1002/fuce.201200072
- Liu, J., and Zenyuk, I. V. (2018). Proton transport in ionomer-free regions of polymer electrolyte fuel cells and implications for oxygen reduction reaction. *Curr. Opin. Electrochem.* 12, 202–208. doi:10.1016/j.coelec.2018.11.015
- Lu, Z., Wilke, K. L., Preston, D. J., Kinefuchi, I., Chang-Davidson, E., and Wang, E. N. (2017). An ultrathin nanoporous membrane evaporator. *Nano Lett.* 17, 6217–6220. doi:10.1021/acs.nanolett.7b02889
- Lv, H., and Mu, S. (2014). Nano-ceramic support materials for low temperature fuel cell catalysts. *Nanoscale* 6, 5063–5074. doi:10.1039/c4nr00402g
- Malik, F., Clement, R., Gethin, D., Kiernan, M., Goral, T., Griffiths, P., et al. (2016). Hierarchical structures of cactus spines that aid in the directional movement of dew droplets. *Phil. Trans. R. Soc. A* 374, 20160110. doi:10.1098/rsta.2016.0110



- Mardle, P., and Du, S. (2022). Introduction to materials for pemfc electrodes. *J. Encycl. Smart Mater.*, 242–255.
- Martinez-Urrutia, A., de Arroiabe, P. F., Ramirez, M., Martinez-Agirre, M., and Bou-Ali, M. M. (2018). Contact angle measurement for libr aqueous solutions on different surface materials used in absorption systems. *Int. J. Refrig.* 95, 182–188. doi:10.1016/j.jrefrig.2018.05.041
- Mashio, T., Sato, K., and Ohma, A. (2014). Analysis of water adsorption and condensation in catalyst layers for polymer electrolyte fuel cells. *Electrochimica Acta* 140, 238–249. doi:10.1016/j.electacta.2014.07.058
- Meng, Q. H., Hao, C., Yan, B., Yang, B., Liu, J., Shen, P. K., et al. (2022). High-performance proton exchange membrane fuel cell with ultra-low loading pt on vertically aligned carbon nanotubes as integrated catalyst layer. *J. Energy Chem.* 71, 497–506. doi:10.1016/j.jechem.2022.03.018
- Middelmann, E. (2002). Improved pem fuel cell electrodes by controlled self-assembly. *Fuel Cells Bull.* 9–12, 9–12. doi:10.1016/s1464-2859(02)11028-5
- MoghadamEsfahani, R. A., Vankova, S. K., Easton, E. B., Ebralidze, I. I., and Specchia, S. (2020). A hybrid pt/nbo/cnts catalyst with high activity and durability for oxygen reduction reaction in pemfc. *Renew. Energy* 154, 913–924. doi:10.1016/j.renene.2020.03.029
- Mu, Y.-T., He, P., Gu, Z.-L., Qu, Z.-G., and Tao, W.-Q. (2022). Modelling the reactive transport processes in different reconstructed agglomerates of a pemfc catalyst layer. *Electrochimica Acta* 404, 139721. doi:10.1016/j.electacta.2021.139721
- Murata, S., Imanishi, M., Hasegawa, S., and Namba, R. (2014). Vertically aligned carbon nanotube electrodes for high current density operating proton exchange membrane fuel cells. *J. Power Sources* 253, 104–113. doi:10.1016/j.jpowsour.2013.11.073
- Muzaffar, T., Kadyk, T., and Eikerling, M. (2018). Tipping water balance and the pt loading effect in polymer electrolyte fuel cells: A model-based analysis. *Sustain. Energy Fuels* 2, 1189–1196. doi:10.1039/c8se00026c
- Newman, J. (1966). Resistance for flow of current to a disk. *J. Electrochem. Soc.* 113, 501–502. doi:10.1149/1.2424003
- Nguyen, H. L., Han, J., Nguyen, X. L., Yu, S., Goo, Y.-M., and Le, D. D. (2021). Review of the durability of polymer electrolyte membrane fuel cell in long-term operation: Main influencing parameters and testing protocols. *Energies* 14, 4048. doi:10.3390/en14134048
- Orfanidi, A., Madkikar, P., El-Sayed, H. A., Harzer, G. S., Kratky, T., and Gasteiger, H. (2017). The key to high performance low pt loaded electrodes. *J. Electrochem. Soc.* 164, F418–F426. doi:10.1149/2.1621704jes
- Ostrovkerk, A., Johánek, V., Dubau, M., Kúš, P., Khalakhan, I., Šmíd, B., et al. (2019). Optimization of ionomer-free ultra-low loading pt catalyst for anode/cathode of pemfc via magnetron sputtering. *Int. J. Hydrogen Energy* 44, 19344–19356. doi:10.1016/j.ijhydene.2018.12.206
- Owejan, J. P., Owejan, J. E., and Gu, W. (2013). Impact of platinum loading and catalyst layer structure on pemfc performance. *J. Electrochem. Soc.* 160, F824–F833. doi:10.1149/2.072308jes
- Owejan, J. P., Trabold, T. A., and Mench, M. M. (2014). Oxygen transport resistance correlated to liquid water saturation in the gas diffusion layer of pem fuel cells. *Int. J. Heat Mass Transf.* 71, 585–592. doi:10.1016/j.ijheatmasstransfer.2013.12.059
- Pan, C., Wu, H., Wang, C., Wang, B., Zhang, L., Cheng, Z., et al. (2008). Nanowire-based high-performance “micro fuel cells”: One nanowire, one fuel cell. *Adv. Mat.* 20, 1644–1648. doi:10.1002/adma.200700515
- Park, J. E., Lim, J., Lim, M. S., Kim, S., Kim, O.-H., Lee, D. W., et al. (2019). Gas diffusion layer/flow-field unified membrane-electrode assembly in fuel cell using graphene foam. *Electrochimica Acta* 323, 134808. doi:10.1016/j.electacta.2019.134808
- Park, J. H., and Aluru, N. M. (2009). Temperature-dependent wettability on a titanium dioxide surface. *Mol. Simul.* 35, 31–37. doi:10.1080/08927020802398884
- Paul, D. K., McCreery, R., and Karan, K. (2014). Proton transport property in supported nafion nanofiber films by electrochemical impedance spectroscopy. *J. Electrochem. Soc.* 161, F1395–F1402. doi:10.1149/2.0571414jes
- Perrins, W., McKenzie, D. R., and McPhedran, R. (1979). Transport properties of regular arrays of cylinders. *Proc. R. Soc. Lond. A. Math. Phys. Sci.* 369, 207–225.
- Perry, M. L., Newman, J., and Cairns, E. J. (1998). Mass transport in gas-diffusion electrodes: A diagnostic tool for fuel-cell cathodes. *J. Electrochem. Soc.* 145, 5–15. doi:10.1149/1.1838202
- Pushkareva, I. V., Pushkarev, A. S., Kalinichenko, V. N., Chumakov, R. G., Soloviev, M. A., Liang, Y., et al. (2021). Reduced graphene oxide-supported pt-based catalysts for pem fuel cells with enhanced activity and stability. *Catalysts* 11, 256. doi:10.3390/catal11020256
- Ramaswamy, N., Gu, W., Ziegelbauer, J. M., and Kumaraguru, S. (2020). Carbon support microstructure impact on high current density transport resistances in pemfc cathode. *J. Electrochem. Soc.* 167, 064515. doi:10.1149/1945-7111/ab819c
- Sabarirajan, D. C., Liu, J., Qi, Y., Perego, A., Haug, A. T., and Zenyuk, I. V. (2020). Determining proton transport in pseudo catalyst layers using hydrogen pump dc and ac techniques. *J. Electrochem. Soc.* 167, 084521. doi:10.1149/1945-7111/ab927d
- Sakai, K., Sato, K., Mashio, T., Ohma, A., Yamaguchi, K., and Shinohara, K. (2009). Analysis of reactant gas transport in catalyst layers; effect of pt-loadings. *ECS Trans.* 25, 1193–1201. doi:10.1149/1.3210674
- Sánchez-Monreal, J., Vera, M., and García-Salaberri, P. A. (2018). Fundamentals of electrochemistry with application to direct alcohol fuel cell modeling” in. *Proton exchange membrane fuel cell*. Rijeka: Intech, 121
- Sánchez-Ramos, A., Gostick, J., and García-Salaberri, P. (2022). Modeling the effect of low pt loading cathode catalyst layer in polymer electrolyte fuel cells. part ii: Parametric analysis. *J. Electrochem. Soc.* 169, 074503. doi:10.1149/1945-7111/ac811d
- Sánchez-Ramos, A., Gostick, J. T., and García-Salaberri, P. A. (2021). Modeling the effect of low pt loading cathode catalyst layer in polymer electrolyte fuel cells: Part i. model formulation and validation. *J. Electrochem. Soc.* 168, 124514. doi:10.1149/1945-7111/ac4456
- Schuler, T., Chowdhury, A., Freiberg, A. T., Sneed, B., Spingler, F. B., Tucker, M. C., et al. (2019). Fuel-cell catalyst-layer resistance via hydrogen limiting-current measurements. *J. Electrochem. Soc.* 166, F3020–F3031. doi:10.1149/2.0031907jes
- Sery, J., and Leduc, P. (2022). Fuel cell behavior and energy balance on board a hyundai nexu. *Int. J. Engine Res.* 23, 709–720. doi:10.1177/14680874211059046
- Shen, S., Cheng, X., Wang, C., Yan, X., Ke, C., Yin, J., et al. (2017). Exploration of significant influences of the operating conditions on the local o<sub>2</sub> transport in proton exchange membrane fuel cells (pemfcs). *Phys. Chem. Chem. Phys.* 19, 26221–26229. doi:10.1039/c7cp04837h
- Siroma, Z., Kakitsubo, R., Fujiwara, N., Ioroi, T., Yamazaki, S.-i., and Yasuda, K. (2009). Depression of proton conductivity in recast nafion® film measured on flat substrate. *J. Power Sources* 189, 994–998. doi:10.1016/j.jpowsour.2008.12.141
- Spingler, F. B., Phillips, A., Schuler, T., Tucker, M. C., and Weber, A. Z. (2017). Investigating fuel-cell transport limitations using hydrogen limiting current. *Int. J. Hydrogen Energy* 42, 13960–13969. doi:10.1016/j.ijhydene.2017.01.036
- Steinbach, A. J., Allen, J. S., Borup, R. L., Hussey, D. S., Jacobson, D. L., Komlev, A., et al. (2018). Anode-design strategies for improved performance of polymer-electrolyte fuel cells with ultra-thin electrodes. *Joule* 2, 1297–1312. doi:10.1016/j.joule.2018.03.022
- Steinbach, A. J., Debe, M. K., Wong, J., Kurkowsky, M. J., Haug, A. T., Peppin, D. M., et al. (2010). A new paradigm for pemfc ultra-thin electrode water management at low temperatures. *ECS Trans.* 33, 1179–1188. doi:10.1149/1.3484611
- Stennett, A. K., Dempsey, G. L., and Gainer, J. L. (2006). trans-sodium crocetinate and diffusion enhancement. *J. Phys. Chem. B* 110, 18078–18080. doi:10.1021/jp064308+
- Straubhaar, B., Pauchet, J., and Prat, M. (2015). Water transport in gas diffusion layer of a polymer electrolyte fuel cell in the presence of a temperature gradient. phase change effect. *Int. J. hydrogen energy* 40, 11668–11675. doi:10.1016/j.ijhydene.2015.04.027
- Sun, X., Yu, H., Zhou, L., Gao, X., Zeng, Y., Yao, D., et al. (2020). Influence of platinum dispersity on oxygen transport resistance and performance in pemfc. *Electrochimica Acta* 332, 135474. doi:10.1016/j.electacta.2019.135474
- Sun, Y., Cui, L., Gong, J., Zhang, J., Xiang, Y., and Lu, S. (2019). Design of a catalytic layer with hierarchical proton transport structure: The role of nafion nanofiber. *ACS Sustain. Chem. Eng.* 7, 2955–2963. doi:10.1021/acssuschemeng.8b03910
- Taherian, F., Marcon, V., van der Vegt, N. F., and Leroy, F. (2013). What is the contact angle of water on graphene? *Langmuir* 29, 1457–1465. doi:10.1021/la304645w
- Takeshita, T., Kamitaka, Y., Shinozaki, K., Kodama, K., and Morimoto, Y. (2020). Evaluation of ionomer coverage on pt catalysts in polymer electrolyte membrane fuel cells by co stripping voltammetry and its effect on oxygen reduction reaction activity. *J. Electroanal. Chem.* 871, 114250. doi:10.1016/j.jelechem.2020.114250
- Talukdar, K., Delgado, S., Lagarteira, T., Gazdzicki, P., and Friedrich, K. A. (2019). Minimizing mass-transport loss in proton exchange membrane fuel cell by freeze-drying of cathode catalyst layers. *J. Power Sources* 427, 309–317. doi:10.1016/j.jpowsour.2019.04.094
- Tellez-Cruz, M. M., Escorihuela, J., Solorza-Feria, O., and Compañ, V. (2021). Proton exchange membrane fuel cells (pemfcs): Advances and challenges. *Polymers* 13, 3064. doi:10.3390/polym13183064

- Thomas, A., Maranzana, G., Didierjean, S., Dillet, J., and Lottin, O. (2014). Thermal and water transfer in pemfcs: Investigating the role of the microporous layer. *Int. J. Hydrogen Energy* 39, 2649–2658. doi:10.1016/j.ijhydene.2013.11.105
- Tomadakis, M. M., and Sotirchos, S. V. (1993). Effective diffusivities and conductivities of random dispersions of nonoverlapping and partially overlapping unidirectional fibers. *J. Chem. Phys.* 99, 9820–9827. doi:10.1063/1.465464
- Ureña, N., Pérez-Prior, M. T., Levenfeld, B., and García-Salaberri, P. A. (2021). On the conductivity of proton-exchange membranes based on multiblock copolymers of sulfonated polysulfone and polyphenylsulfone: An experimental and modeling study. *Polymers* 13, 363. doi:10.3390/polym13030363
- Wang, M., Chen, M., Yang, Z., Liu, G., Lee, J. K., Yang, W., et al. (2019). High-performance and durable cathode catalyst layer with hydrophobic c@ ptfе particles for low-pt loading membrane assembly electrode of pemfc. *Energy Convers. Manag.* 191, 132–140. doi:10.1016/j.enconman.2019.04.014
- Wang, Y., Diaz, D. F. R., Chen, K. S., Wang, Z., and Adroher, X. C. (2020a). Materials, technological status, and fundamentals of pem fuel cells—a review. *Mater. today* 32, 178–203. doi:10.1016/j.mattod.2019.06.005
- Wang, Y., Qiu, B., Fan, S., Liu, J., Qin, Y., Jian, S., et al. (2020b). Membrane distillation of butanol from aqueous solution with polytetrafluoroethylene membrane. *Chem. Eng. Technol.* 43, 1160–1166. doi:10.1002/ceat.201900484
- Weber, A. Z., and Kusoglu, A. (2014). Unexplained transport resistances for low-loading fuel-cell catalyst layers. *J. Mat. Chem. A* 2, 17207–17211. doi:10.1039/c4ta02952f
- Whiston, M. M., Azevedo, I. L., Litster, S., Whitefoot, K. S., Samaras, C., and Whitacre, J. F. (2019). Expert assessments of the cost and expected future performance of proton exchange membrane fuel cells for vehicles. *Proc. Natl. Acad. Sci. U. S. A.* 116, 4899–4904. doi:10.1073/pnas.1804221116
- Wilson, M. S., and Gottesfeld, S. (1992). Thin-film catalyst layers for polymer electrolyte fuel cell electrodes. *J. Appl. Electrochem.* 22, 1–7. doi:10.1007/bf01093004
- Xia, Z., Wang, S., Jiang, L., Sun, H., Liu, S., Fu, X., et al. (2015). Bio-inspired construction of advanced fuel cell cathode with pt anchored in ordered hybrid polymer matrix. *Sci. Rep.* 5, 16100–16111. doi:10.1038/srep16100
- Xie, S., Choi, S.-I., Lu, N., Roling, L. T., Herron, J. A., Zhang, L., et al. (2014). Atomic layer-by-layer deposition of pt on pd nanocubes for catalysts with enhanced activity and durability toward oxygen reduction. *Nano Lett.* 14, 3570–3576. doi:10.1021/nl501205j
- Yarlagadda, V., Carpenter, M. K., Moylan, T. E., Kukreja, R. S., Koestner, R., Gu, W., et al. (2018). Boosting fuel cell performance with accessible carbon mesopores. *ACS Energy Lett.* 3, 618–621. doi:10.1021/acsenerylett.8b00186
- Ye, Q., and Van Nguyen, T. (2007). Three-dimensional simulation of liquid water distribution in a pemfc with experimentally measured capillary functions. *J. Electrochem. Soc.* 154, B1242. doi:10.1149/1.2783775
- Yi, P., Peng, L., Lai, X., Li, M., and Ni, J. (2012). Investigation of sintered stainless steel fiber felt as gas diffusion layer in proton exchange membrane fuel cells. *Int. J. hydrogen energy* 37, 11334–11344. doi:10.1016/j.ijhydene.2012.04.161
- Yoshida, T., and Kojima, K. (2015). Toyota mirai fuel cell vehicle and progress toward a future hydrogen society. *Interface Mag.* 24, 45–49. doi:10.1149/2.f03152if
- Yoshino, S., Shinohara, A., Kodama, K., and Morimoto, Y. (2020). Fabrication of catalyst layer with ionomer nanofiber scaffolding for polymer electrolyte fuel cells. *J. Power Sources* 476, 228584. doi:10.1016/j.jpowsour.2020.228584
- Yunzhe, J., Bowei, Z., Feifei, W., and Mengmeng, L. (2020). “Research on hydrogen energy and fuel cell vehicle roadmap in various countries” in IOP Conference Series: Earth and Environmental Science, 512. IOP Publishing, 012136.
- Zapardiel, D., and García-Salaberri, P. A. (2022). Modeling the interplay between water capillary transport and species diffusion in gas diffusion layers of proton exchange fuel cells using a hybrid computational fluid dynamics formulation. *J. Power Sources* 520, 230735. doi:10.1016/j.jpowsour.2021.230735
- Zenyuk, I. V., Das, P. K., and Weber, A. Z. (2016a). Understanding impacts of catalyst-layer thickness on fuel-cell performance via mathematical modeling. *J. Electrochem. Soc.* 163, F691–F703. doi:10.1149/2.1161607jes
- Zenyuk, I. V., Lamibrac, A., Eller, J., Parkinson, D. Y., Marone, F., Buchi, F. N., et al. (2016b). Investigating evaporation in gas diffusion layers for fuel cells with x-ray computed tomography. *J. Phys. Chem. C* 120, 28701–28711. doi:10.1021/acs.jpcc.6b10658
- Zenyuk, I. V., and Litster, S. (2014). Modeling ion conduction and electrochemical reactions in water films on thin-film metal electrodes with application to low temperature fuel cells. *Electrochimica Acta* 146, 194–206. doi:10.1016/j.electacta.2014.08.070
- Zhang, W., and Pintauro, P. N. (2011). High-performance nanofiber fuel cell electrodes. *ChemSusChem* 4, 1753–1757. doi:10.1002/cssc.201100245
- Zhang, Y., Tao, Y., and Shao, J. (2021). Application of porous materials for the flow field in polymer electrolyte membrane fuel cells. *J. Power Sources* 492, 229664. doi:10.1016/j.jpowsour.2021.229664
- Zhao, J., Shahgaldi, S., Alaefour, I., Xu, Q., and Li, X. (2018). Gas permeability of catalyzed electrodes in polymer electrolyte membrane fuel cells. *Appl. Energy* 209, 203–210. doi:10.1016/j.apenergy.2017.10.087
- Zhao, J., Tu, Z., and Chan, S. H. (2021). Carbon corrosion mechanism and mitigation strategies in a proton exchange membrane fuel cell (pemfc): A review. *J. Power Sources* 488, 229434. doi:10.1016/j.jpowsour.2020.229434
- Zhu, X., Zhang, H., Zhang, Y., Liang, Y., Wang, X., and Yi, B. (2006). An ultrathin self-humidifying membrane for pem fuel cell application: Fabrication, characterization, and experimental analysis. *J. Phys. Chem. B* 110, 14240–14248. doi:10.1021/jp061955s
- Zientara, M., Jakubczyk, D., Litniewski, M., and Hołyst, R. (2013). Transport of mass at the nanoscale during evaporation of droplets: The hertz–knudsen equation at the nanoscale. *J. Phys. Chem. C* 117, 1146–1150. doi:10.1021/jp3091478

## Nomenclature

$A_{Pt}$  Active Pt surface area/m<sup>2</sup>

$A_{geo}$  cell geometric surface area/m<sup>2</sup>

$ASR$  area-specific ohmic resistance/m<sup>2</sup> S<sup>-1</sup>

$a$  active specific surface area/m<sup>-1</sup>

$a_{lv}$  liquid-vapor specific surface area/m<sup>-1</sup>

$C_{O_{2}}$  oxygen concentration/mol m<sup>-3</sup>

$D_{O_{2}}$  oxygen diffusivity in air/m<sup>2</sup> s<sup>-1</sup>

$E_r$  reversible cell voltage/V

**ECSA** electrochemical surface area/m<sup>2</sup> kg<sup>-1</sup>

$F$  Faraday's constant/C mol<sup>-1</sup>

$f$  normalized diffusivity/-

$g$  relative diffusivity/-

$h$  specific enthalpy/J mol<sup>-1</sup>

$I$  surface current density/A m<sup>-2</sup>

$I/C$  ionomer-to-carbon weight ratio/-

$i_{o,c}$  exchange current density of oxygen reduction reaction/A m<sub>Pt</sub><sup>-2</sup>

$j$  volumetric current density/A m<sup>-3</sup>

$K$  permeability/m<sup>2</sup>

$k$  thermal conductivity/W m<sup>-1</sup> K<sup>-1</sup>

$k_H$  dimensionless Henry's constant/-

$L$  pillar spacing/m

$L_{Pt}$  Pt loading/kg<sub>Pt</sub> m<sup>-2</sup>

$l_p$  nanopore spacing/m

$M_i$  molecular mass of species  $i$ /kg mol<sup>-1</sup>

$N_{O_{2}}$  oxygen molar flux/mol m<sup>-2</sup> s<sup>-1</sup>

$N_p$  number of nanopores per ionomer pillar/-

$P$  (geometric) power density/W m<sup>-2</sup>

$P_{Pt}$  Pt-specific power density/W kg<sub>Pt</sub><sup>-1</sup>

$p$  pressure/Pa

$\tilde{p}$  normalized pressure/-

$\dot{Q}$  heat flux/W m<sup>-2</sup>

$R$  radius/m

$R_{O_{2}}$  oxygen transport resistance/s m<sup>-1</sup>

$R_{Pt}$  radius of Pt nanoparticle/m

$R$  nanopore radius/m

$R_v$  secondary pore radius/m

$R^o$  universal gas constant/J mol<sup>-1</sup> K<sup>-1</sup>

$\tilde{R}_i$  ionomer radius ratio/-

**RH** relative humidity/-

$r_f$  roughness factor/-

$s$  water saturation/-

$T$  temperature/K

$t$  time/s

$V_m$  molar volume/m<sup>3</sup> mol<sup>-1</sup>

$V_{cell}$  cell voltage/V

$v_c$  characteristic velocity/m s<sup>-1</sup>

$x$  local coordinate through the nanoporous shell/m

$y$  through-plane coordinate across the CL thickness/m

## Greek letters

$\alpha_c$  transfer coefficient of oxygen reduction reaction/-

$\beta$  dimensionless net transport coefficient of water from anode to cathode/-

$\Gamma$  dimensionless ratio of transport resistances/-

$\gamma$  reaction order of oxygen reduction reaction/-

$\delta$  thickness/m

$\epsilon$  porosity or volume fraction/-

$\eta_c$  cathode overpotential/V

$\theta$  contact angle/-

$\nu$  kinematic viscosity/m<sup>2</sup> s<sup>-1</sup>

$\Pi$  dimensionless factor related to the optimal design point/-

$\rho$  density/kg m<sup>-3</sup>

$\sigma$  conductivity/S m<sup>-1</sup> or surface tension/N m<sup>-1</sup>

$\tau$  tortuosity factor/-

$\phi$  potential/V

$\Omega$  dimensionless ratio of characteristic times or penetration depths/-

## Subscripts and superscripts

**avg** average

**c** cathode or capillary

**ch** channel

**chcl** channel-CL

**cl** catalyst layer

**c + Pt** electron-conductive material + Pt

**d** diffusion

**des** design

**dry** dry conditions

**e** electric

**eff** effective

**flat** flat surface

**g** gas

**geo** geometric

**i** ionomer

**in** inlet

**knud** Knudsen

**l** liquid

**max** maximum

**min** minimum

**mol** molecular

**obs** obstruction

**ohm** ohmic

**opt** optimum

**p** primary nanopore or proton

**pc** phase change

**pem** polymer electrolyte membrane

**prim** primary

**sat** saturation

**sh** shell

**v** viscous

**w** water

**wet** wet conditions